RAMAN SPECTROSCOPY OF MOLD CONIDIA

A Dissertation

by

ZEHUA HAN

Submitted to the Graduate and Professional School of
Texas A&M University
in partial fulfillment of the requirements for the degree of

DOCTOR OF PHILOSOPHY

Chair of Committee,	Alexei V. Sokolov
Committee Members,	Alexey V. Akimov
	Philip R. Hemmer
	M. Suhail Zubairy
Head of Department,	Grigory Rogachev

August 2022

Major Subject: Physics

ABSTRACT

Fungi can be found everywhere in natural and domestic environments and their effects on human activity are numerous and vary widely. Fungi have been used to produce foods, beverages, biofuels, household items, biocatalysts, and so on. However, uncontrolled fungal growth can be costly to human health, agriculture, forestry, and livestock. If they feed on humans, fungi can cause diseases such as ringworm, athlete's foot, lung infections, etc. An example is a fungal/mold overgrowth after a hurricane or flood. The effects on human health may last over years and even lifetimes. In order to prevent damage from mold growth, and minimize the consequences of mold exposure, timely and accurate identification of mold species is required. Conventional methods, like characterizing morphological features or sequencing their genes, are time-consuming and required extensive training. Herein, we apply Raman spectroscopy to identify and characterize mold spore species and demonstrate that the Raman signals originate from melanin molecules within the cell wall. In further studies of 10 mold species, we discover that the main features of Raman spectra of spores correlate with melanin bio-synthesis pathway, find a clue and give a prediction of one species whose synthesis pathway was not well-known before. Finally, we adopt a coherent Raman technique, coherent anti-Stokes Raman spectroscopy, to achieve rapid detection and chemical imaging of mold conidia.

DEDICATION

To my wife and parents

ACKNOWLEDGEMENTS

I would like to express my sincere gratitude to my advisor, Dr. Alexei Sokolov, for his continuous support, guidance and assistance in my doctoral research and study. I'm also grateful to my committee members, Dr. Alexey Akimov, Dr. Philip Hemmer, and Dr. M. Suhail Zubairy, for their guidance and support throughout the course of this research.

I would like to extend my sincere thanks to my colleagues, Dr. Marlan Scully, Dr. Brian Shaw, Dr. Benjamin Strycker, Dr. Aleksei Zheltikov, Dr. Dmitri Voronine, Dr. Volker Decker, Dr. Zhe He, Dr. Yujie Shen, Dr. Zhenhuan Yi, Dr. Kai Wang, Dr. Tao Peng for their advices, knowledge and many insightful discussions as well as suggestions.

Thanks also go to my friends and the department faculty and staff for making my time at Texas A&M University a great experience.

Finally, thanks to my parents for their encouragement and to my wife for her support and love.

CONTRIBUTORS AND FUNDING SOURCES

Contributors

This work was supervised by a dissertation committee consisting of Professor Alexei Sokolov, Professor Alexey Akimov, Professor Philip Hemmer, and Professor M. Suhail Zubairy of the Department of Physics and Astronomy.

All other work conducted for the thesis (or) dissertation was completed by the student independently.

Funding Sources

Graduate study was supported by the Herman F. Heep and Minnie Belle Heep fellowship from Texas A&M University and the Welch Foundation under Grand Number A-1547, and the Stephen E. Harris Professorship in Quantum Optics held by Dr. Alexei Sokolov.

NOMENCLATURE

CARS	Coherent Anti-Stokes Raman Spectroscopy
SERDS	Shifted Excitation Raman Difference Spectroscopy
MM	Minimal Medium
ECDL	External Cavity Diode Laser
AsLS	Asymmetric Least Squares
PCA	Principal Component Analysis
A. nidulans	*Aspergillus nidulans*
A. niger	*Aspergillus niger*
A. flavus	*Aspergillus flavus*
A. fumigatus	*Aspergillus fumigatus*
A. oryzae	*Aspergillus oryzae*
A. versicolor	*Aspergillus versicolor*
A. clavatus	*Aspergillus clavatus*
A. terreus	*Aspergillus terreus*
P. chrysogenum	*Penicillium chrysogenum*
S. chartarum	*Stachybotrys chartarum*

TABLE OF CONTENTS

Page

LIST OF FIGURES

Page

LIST OF TABLES

Page

1. INTRODUCTION

1.1. Background

Fungi (such as molds) are ubiquitous both in indoor and outdoor environments, and their actions upon human health and activity can be costly. Harmful molds that grow within homes and buildings can produce mycotoxins that poison the human body and exacerbate preexisting conditions [1,2]. Within the United States in recent years, mold-related asthma alone has affected approximately 4.6 million people for a total annual cost of $3.5 billion [3]. The agricultural losses from mold damage are also substantial and are estimated to be in the millions of dollars annually for US agri-producers [4]. Consequently, deleterious molds and mycotoxins pose a significant threat to public and economic health and have a large human toll [5].

Minimizing the consequences of mold exposure and damage requires timely and accurate identification of mold species. Fungi are most commonly identified either by characterizing morphological features using light microscopy or by sequencing of housekeeping genes and comparing to genetic repositories [6,7]. Both of these techniques are time consuming and require considerable training for accurate identification. In contrast, Raman spectroscopy of collected mold spores has been proposed as a method to identify fungal species within several minutes. Ghosal et al. have used spontaneous Raman microspectroscopy to measure the spectra of seven mold species and differentiate them from one another [8]. Similarly, Farazkhorasani measured and differentiated between the spontaneous Raman spectra of several strains of *Aspergillus nidulans* (*A. nidulans*) [9].

Surface-Enhanced Raman Spectroscopy (SERS) of the mold species *A. nidulans* has also been reported [9,10]. Therefore, Raman spectroscopy, a robust technique for chemical identification and mapping [11-13], can be implemented for characterization of fungal conidia [14-17].

1.2. Motivation

In order to evaluate and/or prevent damage from mold growth, spore detection and species identification is paramount. We envision the development of a mobile Raman spectroscopy scheme for timely and on-site identification and/or biological characterization. Determination of the relevant experimental and physiological parameters, such as the molecular origin of the Raman signal, is therefore critical. However, the presence of fluorescence emission hinders Raman signals detection, particularly in biological specimens. In general, the cross section of fluorescence is much larger than that of Raman scattering. Therefore, fluorescence can be used for fast imaging and sensitive detection [18- 20]. Compared to fluorescence, Raman signals are always much weaker. Even though near infrared excitation wavelength is applied to significantly suppress the fluorescence emission from bio-samples, Raman peaks are still not obvious. Metallic nanoparticles can enhance Raman response due to localized surface plasmon resonance [21-24], however, they may amplify fluorescence signals as well [25-27]. Additionally, conventional baseline correction method, such as a polynomial function to mimic the fluorescence background, may not be reliable to extract Raman features [15-17]. An easier way to overcome these challenges is Shifted Excitation Raman Difference Spectroscopy (SERDS) [28-33]. The technique relies on the fact that fluorescence is

insensitive to slight change of excitation frequency, while Raman response is and it shifts by the same amount. Utilizing SERDS method, one can separate Raman peaks from fluorescence background. Furthermore, combined SERDS technique with genetic mutants of mold spores, we figure out that the origin of the Raman signals is from melanin (or pigment) molecules within the cell wall [15].

Some mold species have large impact on human health and activity, and some are widely used in medical and industrial production. Investigation of 10 fungal species strongly confirm that the Raman signal results from the melanin pigments bounded within the cell wall. More importantly, the Raman features of spores correlate with the melanin bio-synthesis pathway [16].

Evaluation of mold damage and identification of fungal species also require rapid/real-time analysis and characterization. Compared with spontaneous Raman spectroscopy, coherent Raman spectroscopy like coherent anti-Stokes Raman spectroscopy (CARS) can significantly enhance the Raman scattering efficiency due to molecular coherence. Consequently, CARS signal is stronger by several orders of magnitude. Another advantage over spontaneous Raman spectroscopy is that there is no fluorescence contribution in CARS. Therefore, CARS can be exploited in complex structures such as cells and tissues for rapid detection and chemical imaging.

1.3. Melanin

Melanin is one of the most ancient and widespread biopigments found in almost every kingdom of life [34]. It is found in fossils of dinosaurs, early birds, nonavian theropods, and primitive cephalopods, and as such has been proposed as a biomarker for

the study of evolution [34–36]. As a result of its ancient origin and ubiquity, melanin exhibits a wide range of composition, color, size, occurrence, and function, but may nevertheless be widely defined as a "heterogeneous polymer derived from the oxidation of phenolic or indolic compounds and subsequent polymerization of intermediate phenols and their resulting quinones" [34,37].

In fungi, melanin plays a multi-functional protective role against stress [38]. Melanin protects the fungal organism from ultraviolet, X-ray, gamma-ray, and particulate radiation [39–41]. Melanin allows certain fungi to harvest energy from ionization radiation [42–44]. Melanin protects against desiccation [45] and both heat and cold shock [46,47]. It helps the organism withstand chemical stressors such as hypersaline environments [48], heavy metals [49], hydrolytic enzymes [50], and reactive oxygen species (ROS) [51]. The substantial protective powers of melanin play decisive roles in the virulence of many fungal pathogens [52,53].

1.4. Shifted Excitation Raman Difference Spectroscopy

Shifted Excitation Raman Difference Spectroscopy (SERDS) is designed to separate the Raman and fluorescence contributions in the measured spectra, which occur simultaneously as competing processes, especially in biological specimen (see Figure 1.1). In contrast to fluorescence (Figure 1.1(b)), the Raman response alters significantly even for a small variation in excitation frequency (Figure 1.1(a)), such that different emission frequencies give the same vibrational transition. For fluorescence, identical emission features result from different excitation frequencies. Consequently, the fluorescence contribution can be remarkably suppressed by subtracting one measured spectrum from a

second measured spectrum that has been excited by a slightly shifted laser frequency. The resulting difference spectrum is then dominated by the Raman response. The pure Raman spectrum can then be reconstructed by integrating the difference spectrum.

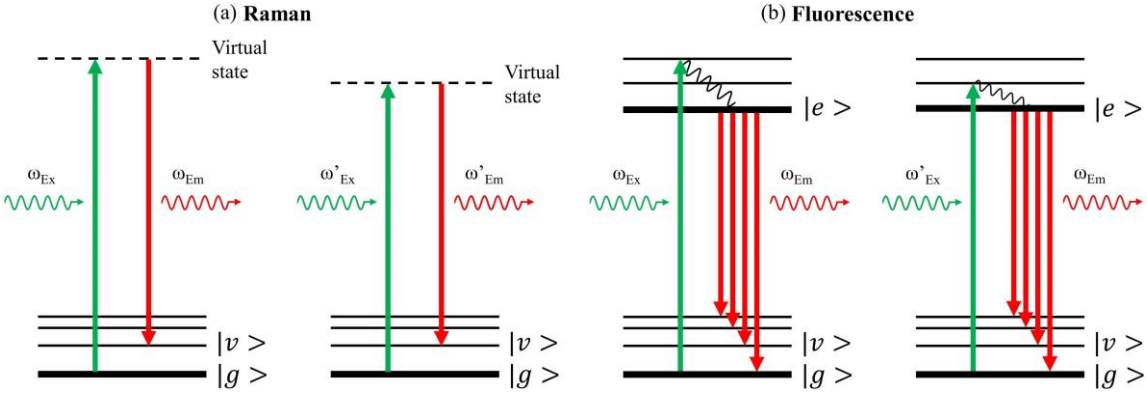

Figure 1.1. Energy diagram in Raman and fluorescence processes. |g >, |v >, and |e > denote ground state, vibrational state, and electronically excited state, respectively. The wavy lines show non-radiative transitions. Greater arrow length denotes higher frequency or higher photon energy, and vice versa. (a) Left panel. In Raman scattering, a molecule is pumped by a laser photon with frequency at ω_{Ex} to a virtual state and then returns to one of its vibrational states, |v >, by emitting a signal photon with lower frequency at ω_{Em}. The vibrational transition matches the frequency difference between input and output photons. Right panel. For the same vibrational transition, a modified, lower pump laser frequency, ω_{Ex}', results in a corresponding signal emission at lower frequency, ω_{Em}'. Thus, the frequencies of Raman features vary as the laser excitation frequency changes. (b) Left panel. In the fluorescence process, the molecule is upconverted to its electronically excited state, |e >, and then decays to the lowest level of the excited state for subsequent fluorescence emission, ω_{Em}. Right panel. A modified pump laser frequency, ω_{Ex}', is relatively lower but still enough for the subsequent fluorescence emission. Fluorescence emission always starts from the lowest level of the excited state, and hence the frequency of fluorescence features will remain the same even if the input laser frequency varies. Consequently, slightly shifting the laser excitation frequency allows separation and detection of the pure Raman signal.

Mathematically, the total signal S recorded by a spectrometer can be expressed with respect to the excitation frequency v_i as

$$S(v,\ v_i) = R(v,\ v_i) + L(v,\ v_i) + B(v)\ , \tag{1}$$

where R, L, and B represent the Raman signal, fluorescence signal, and background signal, respectively.

For two slightly different excitations v_1 and $v_2 = v_1 + \Delta v$, we have

$$S(v,\ v_1) = R(v,\ v_1) + L(v,\ v_1) + B(v)\ , \tag{2}$$

$$S(v,\ v_2) = R(v,\ v_2) + L(v,\ v_2) + B(v)\ . \tag{3}$$

The difference spectrum ΔS can then be derived:

$$\Delta S \equiv S(v,\ v_2) - S(v,\ v_1) = [R(v,\ v_2) - R(v,\ v_1)] + [L(v,\ v_2) - L(v,\ v_1)]\ . \tag{4}$$

Here, we assume that (1) laser power does not change when frequency varies slightly; (2) Raman and fluorescence signals are linearly dependent on laser power; (3) the Raman spectrum shifts the same amount as the laser frequency, while the fluorescence spectrum remains stationary. Then, these assumptions imply:

$$R(v,\ v_2\ ) = R(v,\ v_1 + \Delta v) = R(v + \Delta v,\ v_1)\ , \tag{5}$$

$$L(v,\ v_2) = L(v,\ v_1)\ . \tag{6}$$

Equation (4) then takes the form:

$$\Delta S = R(v,\ v_2) - R(v,\ v_1) = R(v + \Delta v,\ v_1) - R(v,\ v_1) \approx R'(v,\ v_1)\ \Delta v\ , \tag{7}$$

where the prime denotes the derivative with respect to frequency v. In Eq. (7), higher-order terms of Δv are neglected, since Δv itself is assumed to be small. The Raman signal can therefore be reconstructed as

$$R(v, v_1) \approx \int R'(v, v_1)dv = \frac{1}{\Delta v}\int \Delta S dv. \tag{8}$$

We note that the above method is equivalent to "Difference-Integration-δ_Deconvolution" [54].

1.5. References

[1] Zain, M. E. Impact of mycotoxins on humans and animals. J. Saudi Chem. Soc. 2011; 15, 129–144.

[2] Ammann, H. M. Inhalation exposure and toxic effects of mycotoxins in Biology of microfungi (ed. Li, D. W.) 495–523 (Springer, 2016).

[3] Mudarri, D. & Fisk, W. J. Public health and economic impact of dampness and mold. Indoor Air. 2007; 27(3), 226–235.

[4] Leslie, J. F., Bandyopadhyay, R. & Visconti, A. Eds Mycotoxins: Detection Methods, Management, Public Health and Agricultural Trade (Cromwell Press, 2008).

[5] Hamblin, J. The looming consequences of breathing mold. The Atlantic, August 30, https://www.theatlantic.com/health/ archive/2017/08/mold-city/538224/ (2017).

[6] Barnett, H. L. & Hunter, B. B. Illustrated genera of imperfect fungi, 4th edition, 5th printing (APS Press, 2010).

[7] White, T. J. et al. Amplification and direct sequencing of fungal ribosomal RNA genes for phylogenetics in PCR protocols: a guide to methods and applications (ed. Innis, M. A.) 315–322 (Academic Press, 1990).

[8] Ghosal, S., Macher, J. M. & Ahmed, K. Raman microspectroscopy-based identification of individual fungal spores as potential indicators of indoor contamination and moisture-related building damage. Environ. Sci. Technol. 2012; 46(11), 6088–6095.

[9] Farazkhorasani, F. Raman and SERS studies of filamentous fungi. Masters Thesis, University of Manitoba, Winnipeg, Canada, (2014).

[10] Szeghalmi, A., Kaminskyj, S., Rosch, P., Popp, J. & Gough, K. M. Time fluctuations and imaging in the SERS spectra of fungal hypha grown on nanostructured substrates. J. Phys. Chem. B. 2007; 111, 12916–12924.

[11] Schuster, K. C., Reese, I., Urlaub, E., Gapes, J. R. & Lendl, B. Multidimensional information on the chemical composition of single bacterial cells by confocal Raman microspectroscopy. Anal. Chem. 2000; 72(22), 5529–5534.

[12] He, Z. et al. Tip-enhanced Raman imaging of single-stranded DNA with single base resolution. J. Am. Chem. Soc. 2018; 141(2), 753–757.

[13] Chen, Yan, et al. Amphiphilic Zirconium Phosphate Nanoparticles as Tribo-Catalytic Additives of Multi-Performance Lubricants. Journal of Tribology.2022; 144.7.

[14] Strycker, B. et al. CARS spectroscopy of Aspergillus nidulans spores. Scientific reports. 2019; 9(1), 1-7.

[15] Han, Z., et al. Molecular origin of the Raman signal from Aspergillus nidulans conidia and observation of fluorescence vibrational structure at room temperature. Scientific reports. 2020; 10(1), 1-8.

[16] Strycker, B. D., et al. Identification of toxic mold species through Raman spectroscopy of fungal conidia. PloS one. 2020; 15(11), e0242361.

[17] Strycker, B. D., et al. Raman characterization of fungal DHN and DOPA melanin biosynthesis pathways. Journal of Fungi. 2021; 7(10), 841.

[18] Vermot, J., Fraser, S. E., & Liebling, M. Fast fluorescence microscopy for imaging the dynamics of embryonic development. HFSP J. 2008; 2(3), 143–155.

[19] Rajil, N. et al. A fiber optic–nanophotonic approach to the detection of antibodies and viral particles of COVID-19. Nanophotonics. 2021; 10(1), 235-246.

[20] Winter, P. W., & Shroff, H. Faster fluorescence microscopy: advances in high speed biological imaging. Current opinion in chemical biology. 2014; 20, 46–53.

[21] Mayer, K.M. and Hafner, J.H.. Localized surface plasmon resonance sensors. Chemical reviews. 2011; 111(6), pp.3828-3857.

[22] Hutter, E. and Fendler, J.H. Exploitation of localized surface plasmon resonance. Advanced materials. 2004; 16(19), pp.1685-1706.

[23] Peng, T. et al. Enhancing sensitivity of lateral flow assay with application to SARS-CoV-2. Applied Physics Letters. 2020; 117(12), p.120601.

[24] Willets, K.A. and Van Duyne, R.P. Localized surface plasmon resonance spectroscopy and sensing. Annual review of physical chemistry. 2007; 58(1), pp.267-297.

[25] Bauch, M., Toma, K., Toma, M., Zhang, Q. and Dostalek, J. Plasmon-enhanced fluorescence biosensors: a review. Plasmonics. 2014; 9(4), pp.781-799.

[26] He, Z., Han, Z., et al. Quantum plasmonic control of trions in a picocavity with monolayer WS2. Science advances. 2019; 5(10), eaau8763.

[27] Li, J.F., Li, C.Y. and Aroca, R.F. Plasmon-enhanced fluorescence spectroscopy. Chemical Society Reviews. 2017; 46(13), pp.3962-3979.

[28] Shreve, A. P., Cherepy, N. J. & Mathies, R. A. Effective rejection of fluorescence interference in Raman spectroscopy using a shifted excitation difference technique. Appl. Spectrosc. 1992; 46(4), 707–711.

[29] Zhao, J., Carrabba, M. M. & Allen, F. S. Automated fluorescence rejection using shifted excitation Raman difference spectroscopy. Appl. Spectrosc. 2002; 56(7), 834–845.

[30] Sowoidnich, K. & Kronfeldt, H.-D. Shifted excitation Raman difference spectroscopy at multiple wavelengths for in-situ meat species differentiation. Appl. Phys. B. 2012; 108(4), 975–982.

[31] da Silva Martins, M. A. et al. Shifted-excitation Raman difference spectroscopy for in vitro and in vivo biological samples analysis. Biomed. Opt. Express. 2010; 1(2), 617–626.

[32] Matousek, P., Towrie, M. & Parker, A. W. Simple reconstruction algorithm for shifted excitation Raman difference spectroscopy. Appl. Spectrosc. 2005; 59(6), 848–851.

[33] Oshima, Y., Komachi, Y., Furihata, C., Tashiro, H. & Sato, H. Fluorescence-suppressed Raman technique for quantitative analysis of protein solution using a micro-Raman probe, the shifted excitation method, and partial least squares regression analysis. Appl. Spectrosc. 2006; 60(9), 964–970.

[34] Solano, F. Melanins: Skin pigments and much more—types, structural models, biological functions, and formation routes. New J. Sci. 2014; 498276.

[35] Martínez, L.M.; Martinez, A.; Gosset, G. Production of melanins with recombinant microorganisms. Front. Bioeng. Biotechnol. 2019; 7, 285.

[36] Wogelius, R.A.; Manning, P.L.; Barden, H.E.; Edwards, N.P.; Webb, S.M.; Sellers, W.I.; Taylor, K.G.; Larson, P.L.; Dodson, P.; You, H.; et al. Trace metals as biomarkers for eumelanin pigment in the fossil record. Science. 2011; 333, 1622–1626.

[37] Tran-Ly, A.N.; Reyes, C.; Schwarze, F.W.M.R.; Ribera, J. Microbial production of melanin and its various applications. World J. Microbiol. Biotechnol. 2020; 36, 170.

[38] Mattoon, E.; Cordero, R.; Casadevall, A. Fungal melanins and applications in healthcare, bioremediation and industry. J. Fungi. 2021; 7, 488.

[39] Wang, Y.; Casadevall, A. Decreased susceptibility of melanized Cryptococcus neoformans to UV light. Appl. Environ. Microbiol. 1994; 60, 3864–3866.

[40] Khajo, A.; Bryan, R.A.; Friedman, M.; Burger, R.M.; Levitsky, Y.; Casadevall, A.; Magliozzo, R.S.; Dadachova, E. Protection of melanized cryptococcus neoformans from lethal dose gamma irradiation involves changes in melanin's chemical structure and paramagnetism. PLoS ONE. 2011; 6, e25092.

[41] Pacelli, C.; Bryan, R.A.; Onofri, S.; Selbmann, L.; Shuryak, I.; Dadachova, E. Melanin is effective in protecting fast and slow growing fungi from various types of ionizing radiation. Environ. Microbiol. 2017; 19, 1612–1624.

[42] Dadachova, E.; Bryan, R.A.; Huang, X.; Moadel, T.; Schweitzer, A.; Aisen, P.; Nosanchuk, J.D.; Casadevall, A. Ionizing radiation changes the electronic properties of melanin and enhances the growth of melanized fungi. PLoS ONE. 2007; 2, e457.

[43] Robertson, K.L.; Mostaghim, A.; Cuomo, C.; Soto, C.M.; Lebedev, N.; Bailey, R.F.;Wang, Z. Adaptation of the Black YeastWangiella dermatitidis to ionizing radiation: Molecular and cellular mechanisms. PLoS ONE. 2012; 7, e48674.

[44] Pinkert, S.; Zeuss, D. Thermal biology: Melanin-based energy harvesting across the tree of life. Curr. Biol. 2018; 28, R887–R889.

[45] Gorbushina, A.; Kotlova, E.; Sherstneva, O. Cellular responses of microcolonial rock fungi to long-term desiccation and subsequent rehydration. Stud. Mycol. 2008; 61, 91–97.

[46] Cordero, R.J.; Robert, V.; Cardinali, G.; Arinze, E.S.; Thon, S.M.; Casadevall, A. Impact of yeast pigmentation on heat capture and latitudinal distribution. Curr. Biol. 2018; 28, 2657–2664.

[47] Rosas, A.L.; Casadevall, A. Melanization affects susceptibility of Cryptococcus neoformans to heat and cold. FEMS Microbiol. Lett. 1997; 153, 265–272.

[48] Kejžar, A.; Gobec, S.; Plemenitaš, A.; Lenassi, M. Melanin is crucial for growth of the black yeast Hortaea werneckii in its natural hypersaline environment. Fungal Biol. 2013; 117, 368–379.

[49] García-Rivera, J.; Casadevall, A. Melanization of Cryptococcus neoformans reduces its susceptibility to the antimicrobial effects of silver nitrate. Med Mycol. 2001; 39, 353–357.

[50] Bloomfield, B.J.; Alexander, M. Melanins and resistance of fungi to lysis. J. Bacteriol. 1967; 93, 1276–1280.

[51] Jacobson, E.S.; Tinnell, S.B. Antioxidant function of fungal melanin. J. Bacteriol. 1993; 175, 7102–7104.

[52] Smith, D.F.Q.; Casadevall, A. The role of melanin in fungal pathogenesis for animal hosts. In Current Topics in Microbiology and Immunology; Gabler: Wiesbaden, Germany, 2019; Volume 422, pp. 1–30.

[53] Nosanchuk, J.D.; Ovalle, R.; Casadevall, A. Glyphosate inhibits melanization of Cryptococcus neoformansand prolongs survival of mice after systemic infection. J. Infect. Dis. 2001; 183, 1093–1099.

[54] Zhao, J., Carrabba M. M. & Allen, F. S. Automated fluorescence rejection using shifted excitation Raman difference spectroscopy. Appl. Spectrosc. 2002; 56(7) 834-845.

2. MOLECULAR ORIGIN OF THE RAMAN SIGNAL FROM ASPERGILLUS NIDULANS CONIDIA AND OBSERVATION OF FLUORESCENCE VIBRATIONAL STRUCTURE AT ROOM TEMPERATURE*

Successful approaches to identification and/or biological characterization of fungal specimens through Raman spectroscopy may require the determination of the molecular origin of the Raman response as well as its separation from the fluorescence background. The presence of fluorescence can interfere with Raman detection and is virtually impossible to avoid. Fluorescence leads to a multiplicity of problems: one is noise, while another is "fake" spectral structure that can easily be confused for spontaneous Raman peaks. One solution for these problems is Shifted Excitation Raman Difference Spectroscopy (SERDS), in which a tunable light source generates two spectra with different excitation frequencies in order to get rid of fluorescence from the measured signal. We combine a SERDS technique with genetic breeding of mutant populations and demonstrate that the Raman signal from *Aspergillus nidulans* conidia originates in pigment molecules within the cell wall. In addition, we observe unambiguous vibrational fine-structure in the fluorescence response at room temperature. We hypothesize that the vibrational fine-structure in the fluorescence results from the formation of flexible, long-lived molecular cages in the bio-polymer matrix of the cell wall that partially shield target molecules from the immediate environment and also constrain their degrees of freedom.

2.1. Introduction

Raman spectroscopy has been shown to be a robust technique for chemical identification and characterization [1,2]. However, Raman signals are not conspicuous when strong fluorescence emission is present, especially in biological specimens. Therefore, eliminating fluorescence is a challenge in Raman spectroscopy applications. Many techniques have been developed to overcome this challenge, such as time-gated Raman spectroscopy [3] and coherent anti-Stokes Raman spectroscopy (CARS) [4]. However, these methods are costly, require sophisticated designs as well as layouts, and may induce additional problems, such as a non-resonant background in CARS. A simpler approach proposed by Shreve and coworkers is termed Shifted Excitation Raman Difference Spectroscopy (SERDS) [5–10]. This method relies on the fact that the Raman response is sensitive to slight changes in excitation frequency, while the fluorescence response is comparatively insensitive. Consequently, the difference between two measured spectra excited by slightly separated frequencies results in a derivative-like curve. The contribution from fluorescence is suppressed significantly in this difference spectrum, while the Raman contribution remains. Here, we use the same strategy to remove the fluorescence signal from conidia of *Aspergillus nidulans* (*A. nidulans*). We analyzed wild type *A. nidulans* conidia, which are naturally pigmented green, and compared them to two strains carrying pigment production mutations that do not fully form the green pigment and instead produce yellow or white spores. Additionally, conidia that either produced (*rodA*$^{+}$) or lacked (Δ*rodA*) the RodA hydrophobin protein, a dominant feature of the surface of conidia, were also analyzed (see APPENDIX A).

One of our goals in comparing the obtained spectra was to determine the molecular origin of the Raman signal generated using 785 nm excitation radiation, thereby gaining valuable insight into how effective biosensing Raman schemes might be implemented in the future. Our selection of 785 nm excitation radiation in this work is motivated by several factors. Firstly, 785 nm radiation sources are relatively cheap and easy to implement. If Raman analysis of spores is ever to become a viable commercial technique, this must be taken into account. Secondly, 785 nm exhibits a reduced fluorescence response from biological samples. Thirdly, we wish to compare our results to those of previously published works which have also used 785 nm excitation radiation [11,12]. Taking into account both color and the existence/deletion of the RodA protein, we analyzed conidia from a total of six different strains. If the Raman signal originates from pigment molecules within the cell wall, the Raman spectra of different color phenotypes should exhibit marked differentiation. On the other hand, if the Raman signal originates from the surface of the cell wall, which is coated by hydrophobin proteins, the Raman spectra of Δ*rodA* mutants should significantly differ from their corresponding *rodA*$^{+}$ counterparts. As outlined below, our results show that the Raman spectra varied with color phenotype rather than the presence or absence of RodA protein, indicating that the Raman signal originates not from hydrophobin proteins on the surface of the conidia, but rather from the pigments within the cell wall.

In addition, implementation of the SERDS technique has allowed us to observe unambiguous vibrational fine-structure in the fluorescence response at room temperature. This is highly unusual, since cryogenic temperatures are typically required to reduce the

substantial inhomogeneous broadening that obscures the vibrational fine-scale fluorescence structure for molecules embedded in soft or condensed matter [13,14]. In what follows, we detail our results and hypothesize on a plausible mechanism.

2.2. Materials and Methods

2.2.1. Sample Preparation

The green wide-type (WT) strain (A4) was crossed with the white Δ*rodA* strain (FGSC A849) [15] that carries mutants in both the *wA3* (white) and *yA2* (yellow) genes in order to produce both WT and Δ*rodA* with conidia of each of the three possible colors, as previously described [16]. These crosses were carried out on minimal medium (MM) with appropriate supplements. Each strain was evaluated based on previously published protocols [17] for hydrophobicity to determine if it contained Δ*rodA*. Progeny were collected that displayed all six possible phenotypes: green, $rodA^+$; green, Δ*rodA*; yellow, $rodA^+$; yellow, Δ*rodA*; white, $rodA^+$; and white, Δ*rodA*. To collect spores, each of the six strains was grown on an individual MM plate for seven days at 30 °C, then harvested with 1 mL sterile distilled water and a bent glass rod, for a final concentration of 1×10^6 spores. Spore suspensions were kept at 4 °C while not in use, and adequately vortexed prior to preparing for experiments.

2.2.2. SERDS Experiments

The preparation of spore samples for subsequent Raman interrogation was completed as follows. First, ~6 μL of the spore suspension was pipetted onto the surface of an uncoated ultraviolet fused silica window (WG41010, Thorlabs). The water in the suspension was then allowed to evaporate over the course of several hours, leaving the

spores as a deposit on the surface of the silica window. The spore sample on the silica window was then placed beneath a long-working-distance objective (HCX PL Fluotar, 100×, N.A. 0.75, Leica) in a commercial confocal Raman microscope (LabRAM HR Evolution, Horiba). The light source was a homemade external cavity diode laser (ECDL) operating at ~785 nm. A bandpass filter was inserted to clean the laser spectrum. Beam power was optimized to avoid burning the spore samples while maximizing the optical signal and was therefore set at ~0.87 mW. The Raman radiation was collected in the epi-direction (see Fig. 2.1(a)) and, after passing through an edge filter, propagated through the confocal slit (set to 200 μm), reflected off the spectrometer grating (150 gr/mm), and finally detected by an EMCCD (Synapse 354308, Horiba Jobin Yvon Inc.). Two spectra of a single spore excited by two different frequencies were recorded separately, the second immediately after the first. In order to increase the signal-to-noise ratio, each spectrum was taken as the average of 12 accumulations of 5-second acquisitions, for a total integration time of 60 seconds. Figure 2.1(b) demonstrates energy level diagrams of processes of Raman scattering and fluorescence in a molecular system.

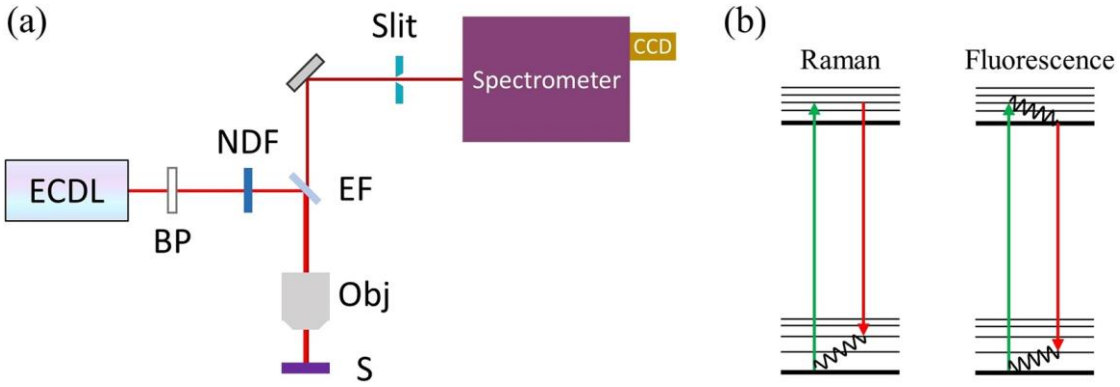

Figure 2.1. (a) Simplified schematic of SERDS experimental layout. ECDL: external cavity diode laser; BP: bandpass filter; NDF: neutral density filter; EF: edge filter;

Obj: microscope objective; S: sample. (b) Diagrams of Raman scattering and fluorescence in a molecular system containing both electronic ground and excited states with multiple vibrational modes. Here, we assume that the excited electronic state contains a continuum of vibrational modes. The wavy lines indicate non-radiative decay.

2.3. Results and Discussion

For each of the three possible color phenotypes (green, yellow and white, respectively) of *A. nidulans* conidia, we analyzed 100 individual spores of *rodA*$^{+}$ and 100 individual spores of Δ*rodA*. Within a given color phenotype, the Raman spectrum of the *rodA*$^{+}$ is identical to that of its corresponding Δ*rodA* strain. The remainder of this work therefore focuses only on strains that are *rodA*$^{+}$. Raman data for each of three possible color phenotypes are shown in Fig. 2.2. It can be inferred that the genotype of all strains discussed from this point on are *rodA*$^{+}$ strains unless otherwise specified. We point out that the measured raw spectra shown in Fig. 2.2 contain many fringe-like minor peaks that have the same spectral width as Raman peaks but which, in contrast to a genuine Raman response, are insensitive to slight changes in excitation frequency. We have taken care to establish that these minor peaks do not originate from any systematic instrumental response. On the contrary, they are indicative of the light-matter interaction between the laser excitation and the molecules within the conidia. Because these minor peaks are insensitive to slight changes in excitation frequency, we conclude that they originate from the fluorescence response. Also, because they are superimposed over a much broader fluorescence background, we describe them using the term “fine-scale”. We demonstrate that a SERDS technique can separate these fine-scale fluorescence features from the

Raman spectrum, while a conventional Asymmetric Least Squares (AsLS) background subtraction algorithm cannot [18].

Figure 2.2(a) shows the normalized raw data of a single green spore excited by two slightly different frequencies. Each normalized raw spectrum was obtained by dividing the whole signal integrated from 250 cm^{-1} to 2600 cm^{-1} and then rescaling between 0 and 1, unless otherwise mentioned. We note that the frequency shift Δv is not a bounded parameter in the SERDS method. Many studies have shown that the optimal value of Δv should be comparable to the full-width-at-half-maximum (FWHM) of the major peaks [6,8]. Here, we set the frequency shift of the two excitation wavelengths (784.2628 nm and 785.8203 nm, respectively) to be ~25.2 cm^{-1}, which is close to the bandwidth of the most prominent peak at ~1641 cm^{-1}. Green spores exhibit strong fluorescence with four main peaks and a few minor peaks. Farazkhorasani [12] has identified the main peak at ~1641 cm^{-1} as belonging to the Amide I C = C stretching mode. It should be noted that the molecular structure of the green pigment in *A. nidulans* is still unknown [19]. However, based upon its Raman spectrum, it should be expected that it contains an Amide group. The fluorescence background in the two measurements shown is almost identical, while several of the peaks are shifted. The reconstructed Raman spectrum shown in Fig. 2.2(b) (red curve) is generated through integration of the difference spectrum between two curves in Fig. 2.2(a). Conventional background-subtracted spectra (bottom curves in Fig. 2.2(b)) are also generated using the AsLS algorithm developed by Eilers and Boelens [18] for comparison. The main difference between the two techniques is located in the region beyond 1700 cm^{-1}. The restored Raman spectrum generated with the SERDS method

shows no bands in this range. On the other hand, baseline-corrected spectra using the AsLS method display distinct and reproducible features in this region. However, these features remain unchanged as excitation frequency shifts, proving that they do not belong to Raman bands and are artifacts of fluorescence. Similar results are exhibited in the other 99 examined spores.

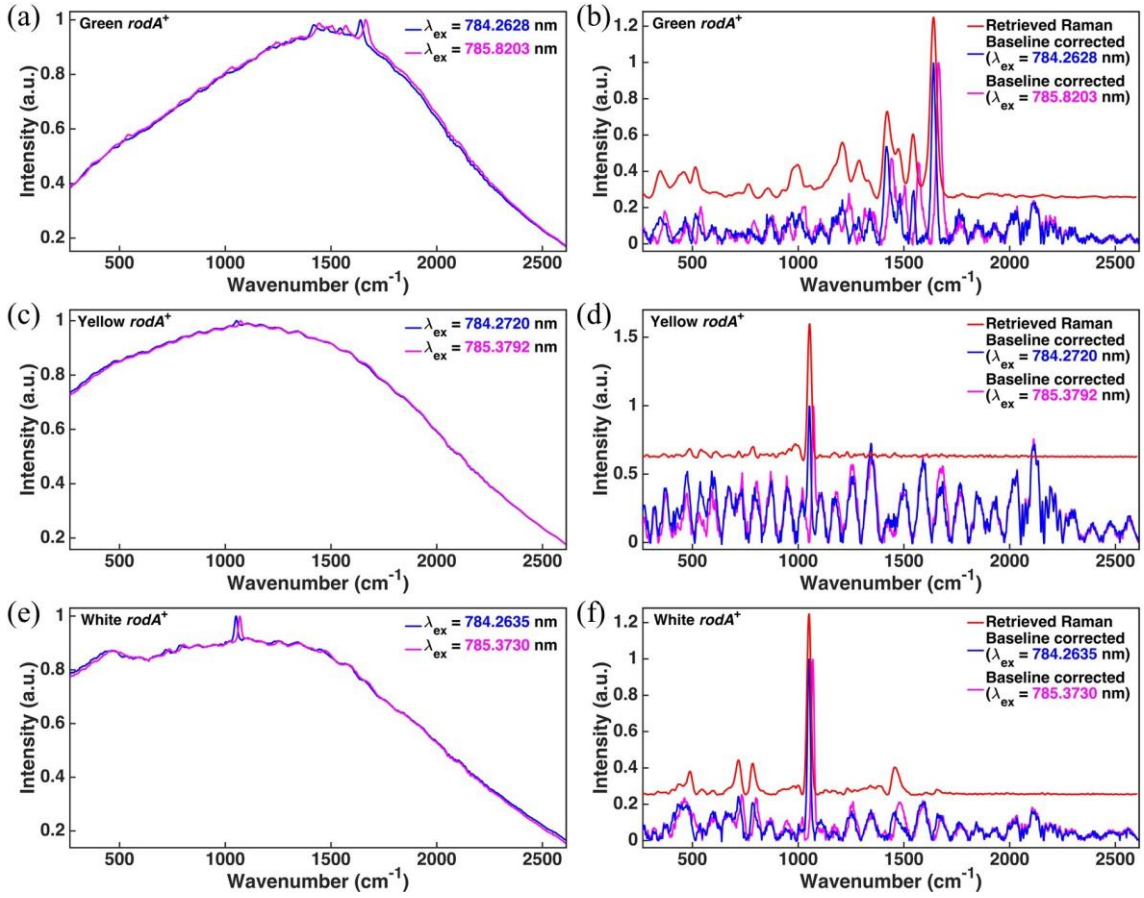

Figure 2.2. Spectra of color phenotypes and the corresponding SERDS spectra. The top (a, b), middle (c, d), and bottom (e, f) rows correspond to green, yellow, and white color phenotypes, respectively. The left column (a, c, e) corresponds to raw measured spectra taken with two slightly different laser excitation wavelengths. The right column (b, d, f) shows the corresponding reconstructed Raman spectrum (top red curve in each frame) retrieved using the SERDS technique compared to spectra generated from a conventional Asymmetric Least Squares (AsLS) algorithm (bottom curves in each frame). For the baseline-corrected spectra, only those features in each

spectrum that correspond to a Raman response are sensitive to slight changes in laser excitation frequency.

Figure 2.2(c) shows the normalized average raw data of 100 yellow spores with two different excitation wavelengths at ~785 nm. Here, the averaged raw data are used in order to improve the signal-to-noise ratio, which is otherwise low for a single spore. We set the shift of the two excitation frequencies to be ~18.0 cm^{-1}, which is close to the bandwidth of the peak at ~1055 cm^{-1}. Yellow spores have a strong fluorescence background and a small peak at ~1055 cm^{-1} that most likely corresponds to a C-O stretching mode [12]. The fluorescence signals in the two measurements are almost identical, while the peak exhibits a shift. The reconstructed Raman spectrum in Fig. 2.2(d) (red curve) is generated by integrating the SERDS spectrum resultant from the spectra in Fig. 2.2(c). Also shown in Fig. 2.2(d) are conventional background-subtracted spectra (bottom curves) generated from the same data for comparison. As can be clearly seen, the two techniques manifest distinct differences. The restored Raman spectrum using the SERDS method shows only one noticeable band in the whole range. In contrast, the baseline-corrected spectra using the AsLS method present many features that remain unchanged as excitation frequency shifts, proving once again that they do not belong to Raman bands but in fact result from a fine-scale fluorescence response.

Figure 2.2(e) shows the normalized average raw data of 100 white spores. Once again, the averaged raw data are used in order to improve the signal-to-noise ratio, which is otherwise low for a single spore. Two different excitation wavelengths at ~785 nm were used, with a corresponding frequency shift of ~18.0 cm^{-1}. White spores exhibit strong

fluorescence along with a small peak at ~1051 cm^{-1}. The reconstructed Raman spectrum shown in Fig. 2.2(f) (red curve) is generated from the integration of the SERDS spectrum resultant from the data in Fig. 2.2(e). Also shown in Fig. 2.2(f) are conventional background-subtracted spectra (bottom curves) generated from the same data for comparison. The restored Raman spectrum using the SERDS method shows one noticeable band at ~1051 cm^{-1} and two small bands at ~717 cm^{-1} and 785 cm^{-1}, respectively. The peak at ~1051 cm^{-1} most likely corresponds to a C-O stretching mode [12]. The small bands at ~717 cm^{-1} and 785 cm^{-1} may tentatively be identified as belonging to phospholipid C-N stretching and O-P-O stretching, respectively [20]. As in the cases of green and yellow conidia, the baseline-corrected spectra of white conidia exhibit many features that remain unchanged as the excitation frequency shifts, proving that they are in fact fine-scale features of the fluorescence response.

Taking into account all of the above, it can be concluded that the measured Raman spectrum originates not from the hydrophobin proteins on the surface of the conidia but rather from the pigments within the cell wall, which result in each color phenotype. Our results are indicative of the biosynthetic pathway that produces each of the pigments. The white (*wA3*) and yellow (*yA2*) color phenotypes exist as mutations of the wild green phenotype and correspond to various stages of the pigment-producing process. An enzyme (WA) converts the white pigment molecule into the yellow pigment molecule, while an additional enzyme (YA) converts the yellow pigment molecule into the green pigment molecule, whose chemical structure is still unknown [19]. The green phenotype is expressed if the entire biosynthetic pathway is completed, while the white and yellow

phenotypes are arrested at their corresponding stages. Our results show that the Raman spectrum of the white phenotype is noticeably different from that of the yellow phenotype, confirming a differing molecular composition and/or structure. Likewise, the Raman spectrum of the green phenotype is drastically different from both the white and the yellow phenotypes, again confirming a unique molecular composition and/or structure.

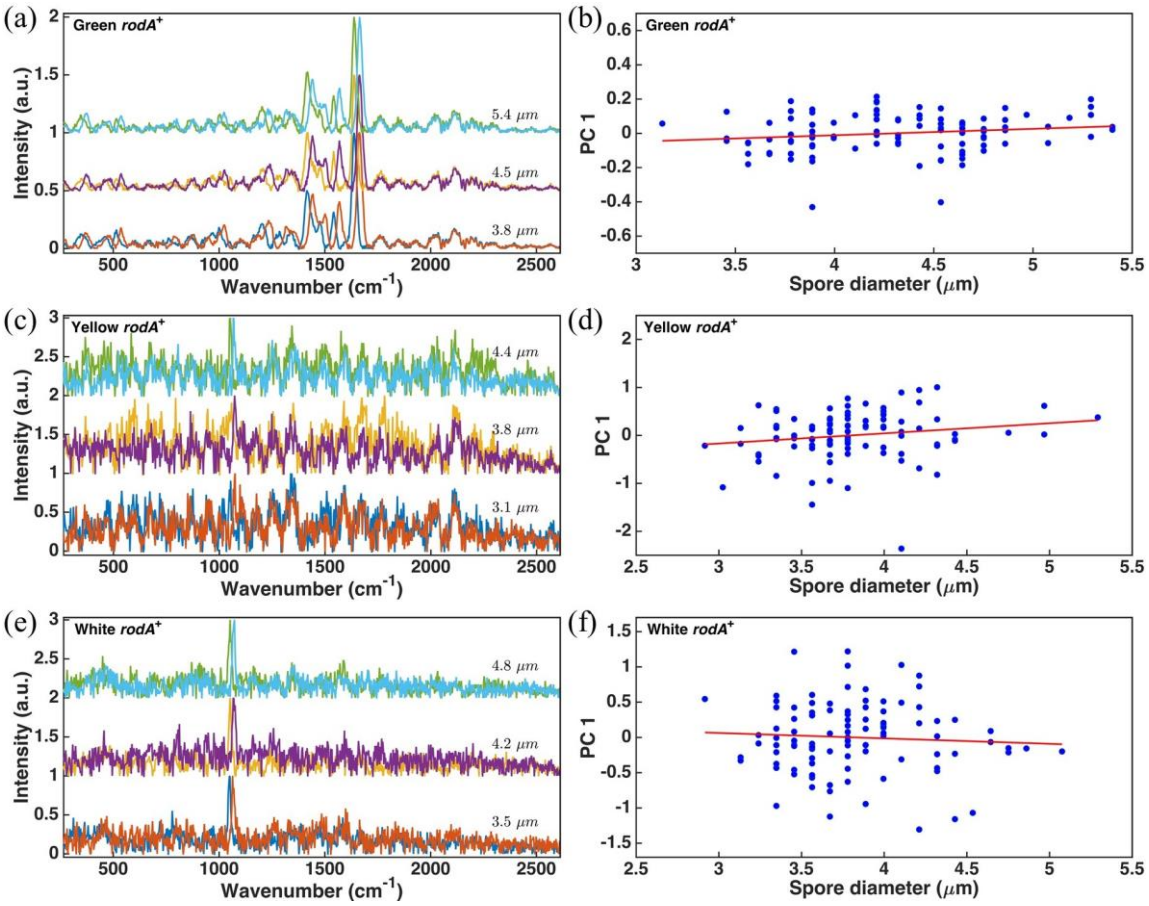

Figure 2.3. The fine-scale fluorescence spectra of three species with different spore diameter and the first principal component of the fine-scale fluorescence of 100 conidia against their size. The numbers close to curves in (a), (c), (e) are the size of corresponding measured spores. In order to increase signal-to-noise ratio, spectra in (c) and (e) are averaged over the number of spores with the same size.

The existence of fine-scale fluorescence features in the measured raw spectra that are otherwise indistinguishable from Raman peaks has no well-documented explanation. It can be seen from Fig. 2.2 that the spectral shape of the fine-scale fluorescence appears to be roughly periodic in nature. We have taken care to eliminate the possibility that these features might result from an instrumental or systematic anomaly in our equipment. One might suspect that the periodic structure results from spectral interference due to the changes in refractive index at the boundaries of the spore, but in fact the periodic spectral structure is almost identical in spores from the same population sample regardless of spore size, as shown in Fig. 2.3.

In order to determine if the size of the spores affects the fine-scale fluorescence, the spectra of each color phenotype obtained with slightly shifted excitation wavelengths have been plotted in Fig. 2.3(a,c,e). The spectra of each spore were obtained by subtracting its corresponding baseline using AsLS and then plotted according to different spore diameters. The diameter of each spore was measured according to the largest horizontal dimension. In addition, in Fig. 2.3(c,e), an average was taken over the spectra obtained from spores with diameters within ± 0.1 μm of the listed diameter in order to increase signal-to-noise ratio. The curves in Fig. 2.3(a,c,e), respectively, demonstrate that there is no distinct difference in the fine-scale fluorescence of each color phenotype as the spore diameter varies. Principal component analysis (PCA) of 100 spores of each color phenotype was also conducted in order to quantify the relationship of the fine-scale fluorescence to the spore diameter. Here, the spectrum corresponding to the lower excitation wavelength of each spore was used to construct a data matrix for PCA analysis

with a MATLAB software package (*pca* function) [21]. For convenience, we consider the fine-scale fluorescence located in the range from 1730 to 2600 cm^{-1}. Figure 2.3(b,d,f) plot the PC score of the first principal component versus its corresponding spore diameter for different color phenotypes. The dependence of the fine-scale fluorescence on spore diameter is very weak. For example, the variation of fine-scale fluorescence in spore diameter has a Pearson correlation coefficient of $\rho = 0.1667$ with $R^2 = 0.0278$ for green conidia and that of $\rho = 0.1694$ with $R^2 = 0.0287$ for yellow conidia. In contrast, the fine-scale fluorescence of white conidia is even less dependent on spore diameter with $\rho = -0.0635$ and $R^2 = 0.0050$. It is obvious that there is no correlation between fine-scale fluorescence and spore diameter in any color phenotype.

In addition, it is known that 785 nm radiation is efficiently scattered from the carbohydrates in cell walls, giving rise to the well-known red-edge effect of vegetation spectroscopy. Consequently, there are no surface waves to generate a corresponding spectral interference by propagating around the circumference of the spore. Finally, the spore diameter itself, 3 to 5 μm, is of the same order of magnitude as the wavelength of light used to interrogate it. It is simply impossible to account for the pathlength difference required to form the number of periodicities observed in the 1700 to 2500 cm^{-1} range of Fig. 2.2. It must be concluded, therefore, that these fine-scale spectral features do in fact result from a fundamental energy structure in the fluorescence response due to fluorescent radiative decay from the electronic excited state to various vibrational energy levels in the electronic ground state.

This conclusion, however, challenges current understandings of molecular dynamics in soft and condensed matter systems. It is widely acknowledged that molecules embedded in liquid or solid environments at room temperature do not exhibit vibrational fine-structure in their fluorescence spectra due to the substantial inhomogeneous broadening that obscures these fine-scale features [13,14]. The fact that we clearly observe vibrational fine-structure in the fluorescence response from molecules embedded in the cell wall of spores requires an unconventional explanation.

One possible explanation for the observed vibrational fine-structure in the fluorescence may be the formation of long-lived molecular cages in the bio-polymer matrix of the cell wall, as explored by Cicogna *et al*. [22] and Prampolini *et al*. [23]. In these works, it was observed that chromophores embedded in polymer matrices exhibited vibrational fine-structure in their fluorescence spectra. Subsequently, through detailed discrete Fourier transform calculations, it was found that fluorescent molecules enclosed within a flexible cage-like structure formed by the polymer bundle were both partially shielded from direct interaction with the immediate environment and also slightly constrained in vibrational degrees of freedom, thus reducing the amount of inhomogeneous broadening that would otherwise obscure the vibrational structure in the fluorescence spectrum [22]. It is probable that these same physical conditions are prevalent within the cell wall of *A. nidulans*, which is largely composed of an extensively cross-linked glucan, chitin, and glycoprotein bio-polymer [24].

If so, our unambiguous measurements of vibrational fine-structure in the fluorescence spectra of molecules embedded in conidia cell walls may provide the first

observations of a possible mechanism for the allowance of long-lived quantum coherences in biological systems. Bio-polymers are ubiquitous in nature. It is not impossible that long-lived molecular cages play an important role in avian, insect, and plant magnetoreception [25,26], for which coherence times as long as 10 μs may be required [27].

2.4. Conclusion

We have used the SERDS technique to successfully retrieve the Raman spectra of conidia of three possible color phenotypes of *rodA*$^{+}$ strains in *A. nidulans*, as well as their corresponding Δ*rodA* strains. Our data indicate that, with an excitation wavelength of 785 nm, the Raman spectra of *A. nidulans* green *rodA*$^{+}$ conidia originate in the pigment molecules within the cell wall. While the 785 nm wavelength used to generate Raman spectra in this work cannot distinguish *rodA*$^{+}$ conidia from their Δ*rodA* counterparts, it may be possible to differentiate between *rodA*$^{+}$ and Δ*rodA* conidia of the same color using a laser excitation frequency in the ultraviolet, since Raman scattering from proteins is resonantly enhanced in this regime.

In our experiments the SERDS technique requires a total acquisition time of 120 s compared to a 1 s dwell time in CARS experiments [4], limiting its applications in fast imaging of biological samples such as observations of molecular dynamics. In addition, the quality of the spectral reconstruction depends on the amount of noise in the raw data. However, averaging over many samples as we have done here can increase the signal-to-noise level.

It should be noted that our measurements demonstrate SERDS has a distinct advantage over conventional baseline correction methods and that it is much more reliable

and accurate. Baseline correction is unable to exclude fine-scale features in the measured spectrum that result from the fluorescence response, thus making the technique suspect when analyzing biological samples of the kind described in this work. In particular, software packages such as those used by both Ghosal *et al*. [11] and Farazkhorasani [12] may include erroneous fluorescence features in the retrieved spectrum. SERDS, on the other hand, can eliminate these fluorescence features from the measured spectrum because, in contrast to the desired Raman response, even the fine-scale fluorescence is insensitive to slight changes in the excitation frequency.

Finally, through implementation of the SERDS technique, we have unambiguously measured vibrational fine-structure in the fluorescence response of molecules embedded in conidia cell walls at room temperature. We hypothesize that this unusual result may be due to the formation of flexible, long-lived molecular cages within the bio-polymer of the cell wall, and that this effect may possibly play an important role in biological processes for which long-lived quantum coherence is required.

2.5. References

[1] Schuster, K. C., Reese, I., Urlaub, E., Gapes, J. R. & Lendl, B. Multidimensional information on the chemical composition of single bacterial cells by confocal Raman microspectroscopy. Anal. Chem. 2000; 72(22), 5529–5534.

[2] He, Z. et al. Tip-enhanced Raman imaging of single-stranded DNA with single base resolution. J. Am. Chem. Soc. 2018; 141(2), 753–757.

[3] Tahara, T. & Hamaguchi, H.-O. Picosecond Raman spectroscopy using a streak camera. Appl. Spectrosc. 1993; 47(4), 391–398.

[4] Strycker, B. D. et al. CARS spectroscopy of Aspergillus nidulans spores. Scientific Reports. 2019; 9, 1789.

[5] Shreve, A. P., Cherepy, N. J. & Mathies, R. A. Effective rejection of fluorescence interference in Raman spectroscopy using a shifted excitation difference technique. Appl. Spectrosc. 1992; 46(4), 707–711.

[6] Zhao, J., Carrabba, M. M. & Allen, F. S. Automated fluorescence rejection using shifted excitation Raman difference spectroscopy. Appl. Spectrosc. 2002; 56(7), 834–845.

[7] Sowoidnich, K. & Kronfeldt, H.-D. Shifted excitation Raman difference spectroscopy at multiple wavelengths for in-situ meat species differentiation. Appl. Phys. B. 2012; 108(4), 975–982.

[8] da Silva Martins, M. A. et al. Shifted-excitation Raman difference spectroscopy for in vitro and in vivo biological samples analysis. Biomed. Opt. Express. 2010; 1(2), 617–626.

[9] Matousek, P., Towrie, M. & Parker, A. W. Simple reconstruction algorithm for shifted excitation Raman difference spectroscopy. Appl. Spectrosc. 2005; 59(6), 848–851.

[10] Oshima, Y., Komachi, Y., Furihata, C., Tashiro, H. & Sato, H. Fluorescence-suppressed Raman technique for quantitative analysis of protein solution using a micro-Raman probe, the shifted excitation method, and partial least squares regression analysis. Appl. Spectrosc. 2006; 60(9), 964–970.

[11] Ghosal, S., Macher, J. M. & Ahmed, K. Raman microspectroscopy-based identification of individual fungal spores as potential indicators of indoor contamination and moisture-related building damage. Environ. Sci. Technol. 2012; 46(11), 6088–6095.

[12] Farazkhorasani, F. Raman and SERS studies of filamentous fungi. Masters Thesis, University of Manitoba, Winnipeg, Canada (2014).

[13] Valeur, B. Molecular Fluorescence: Principles and Applications. (Wiley-VCH, 2002).

[14] Turro, N.J. Modern Molecular Photochemistry. (University Science Books, 1991).

[15] McCluskey, K., Wiest, A. & Plamann, M. The Fungal Genetics Stock Center: a repository for 50 years of fungal genetics research. J. Biosciences.2010; 35(1), 119–126.

[16] Kaminskyj, S. G. Fundamentals of growth, storage, genetics and microscopy of Aspergillus nidulans. Fungal Genetics Reports. 2001; 48(1), 25–31.

[17] Grunbacher, A. et al. Six hydrophobins are involved in hydrophobin rodlet formation in Aspergillus nidulans and contribute to hydrophobicity of the spore surface. PLOS ONE. 2014; 9(4), e94546.

[18] Eilers, P. H. & Boelens, H. F. Baseline Correction with Asymmetric Least Squares Smoothing. Leiden Univeristy Medical Centre Report. 2005, 1, 5.

[19] Klejnstrup, M. L. et al. Genetics of polyketide metabolism in Aspergillus nidulans. Metabolites. 2012; 2(1), 100–133.

[20] Talari, A. C. S., Movasaghi, Z., Rehman, S. & Rehman, I. Raman spectroscopy of biological tissues. Appl. Spectrosc. Rev. 2015; 50(1), 46–111.

[21] Matlab R2015b, The MathWorks, Inc., Natick, Massachusetts, United States.

[22] Cicogna, F., Coiai, S., Pinzino, C., Ciardelli, F. & Passaglia, E. Fluorescent polyolefins by free radical post-reactor modification with functional nitroxides. React. Funct. Polym. 2012; 72, 695–702.

[23] Prampolini, G., Monti, S., De Mitri, N. & Barone, V. Evidences of long lived cages in functionalized polymers: effects on chromophore dynamic and spectroscopic properties. Chem. Phys. Lett. 2014; 601, 134–138.

[24] Bowman, S. M. & Free, S. J. The structure and synthesis of the fungal cell wall. BioEssays. 2006; 28, 799–808.

[25] Lloyd, S. Quantum coherence in biological systems. J. Phys.: Conf. Ser. 2011; 302, 012037.

[26] Galland, P. & Alexander, P. Magnetoreception in plants. J. Plant Res. 2005; 118, 371–389.

[27] Gauger, E. M., Rieper, E., Morton, J. J., Benjamin, S. C. & Vedral, V. Sustained quantum coherence and entanglement in the avian compass. PRL. 2011; 106, 040503.

3. IDENTIFICATION OF TOXIC MOLD SPECIES THROUGH RAMAN SPECTROSCOPY OF FUNGAL CONIDIA[*]

We use a 785 nm shifted excitation Raman difference (SERDS) technique to measure the Raman spectra of the conidia of 10 mold species of especial toxicological, medical, and industrial importance, including *Stachybotrys chartarum*, *Penicillium chrysogenum*, *Aspergillus fumigatus*, *Aspergillus flavus*, *Aspergillus oryzae*, *Aspergillus niger*, and others. We find that both the pure Raman and fluorescence signals support the hypothesis that for an excitation wavelength of 785 nm the Raman signal originates from the melanin pigments bound within the cell wall of the conidium. In addition, the major features of the pure Raman spectra group into profiles that we hypothesize may be due to differences in the complex melanin biosynthesis pathways. We then combine the Raman spectral data with neural network models to predict species classification with an accuracy above 99%.

3.1. Introduction

In a previous work, our group measured the Raman signature of *Aspergillus nidulans* (*A. nidulans*) using Coherent Anti-Stokes Raman Spectroscopy (CARS) an order of magnitude faster than spontaneous Raman techniques [1]. One disadvantage to doing so, however, is the comparative cost and complexity of a CARS setup in relation to a simpler, more robust, and initially more mobile spontaneous Raman scheme. Even so, we subsequently showed that even a simple spontaneous Raman scheme has its own pitfalls

[2]. Using Shifted Excitation Raman Difference Spectroscopy (SERDS), we separated the genuine Raman signal from spurious "fake" fine-scale fluorescence features that also appear in the spectrum and that a naïve analysis would misidentify as belonging to particular molecular vibration modes. We also showed that for an excitation wavelength of 785 nm the Raman signal of *A. nidulans* conidia originates from pigment molecules within the cell wall [2]. While this suggests that the same is likely to be true for conidia of other species, as well, it begs the question of whether 785 nm excitation will be able to yield a useful Raman signal in all cases, since the pigmentation of mold species is highly variable.

For the interrogation of biological samples, 785 nm excitation is often considered to be optimal, since it reduces the obscuring fluorescence excited by shorter wavelengths and yet may still be detected with conventional charge-coupled device (CCD) technology, which has limited sensitivity for longer infrared wavelengths [3]. Previous works demonstrated that a spontaneous 785 nm Raman scheme can characterize a handful of readily available and benign mold species [2, 4, 5]. But can a spontaneous 785 nm Raman scheme be used to characterize the particular mold species that are known to be of especial toxicological, medical, or industrial importance? And, if so, what kind of technique is required to accurately identify and differentiate them? These are the questions that guide the present work. Here, we analyze the Raman spectra of ten mold species using the SERDS technique and quantify the level of interspecies differentiation in order to determine necessary experimental practices.

The mold species have been chosen for their medical, industrial, and scientific interest. They are species which have a large impact on human life and activity. *Stachybotrys chartarum* (*S. chartarum*), the infamous "black mold," has received increased popular attention in recent decades on account of the human health effects of the mycotoxins that it produces [6, 7]. It is a common contaminant of damp buildings [8]. *Penicillium chrysogenum* (*P. chrysogenum*) is used in the bulk industrial production of penicillin [9]. It is also a common contaminant of damp buildings [8]. Eight different species from the genus *Aspergillus* were selected in order to assess whether closely related species could be differentiated using SERDS [10]. *Aspergillus fumigatus* (*A. fumigatus*), whose airborne conidia are among the most prevalent worldwide, is the fungus responsible for 90% of aspergillosis cases, the infectious colonization of the lungs in immunocompromised individuals [11–13]. *Aspergillus niger* (*A. niger*) is an important industrial fungus used in the production of citric acid and of enzymes such as amylases (for example glucoamylase, which is used in producing corn syrup), pectinases (used to clarify cider and wine), and proteases (used in detergents) [14–16]. It may also cause aspergillosis [11]. *Aspergillus oryzae* (*A. oryzae*) has been used for thousands of years in food and beverage fermentation. Its preparation is commonly known as koji. Among other products, it is used to produce sake, soy sauce, and miso on industrial scales, each of which is worth billions of dollars annually [17, 18]. *Aspergillus flavus* (*A. flavus*) is of great economic importance as a pathogen in pre- and post-harvest agricultural crops such as corn, peanuts, cotton, and treenuts [19]. It produces Aflatoxin B1, the most potent naturally occurring carcinogen and one of the few mycotoxins to have been developed as

a biological weapon [20]. *A. flavus* may also cause aspergillosis [11]. *Aspergillus terreus* (*A. terreus*) is known to produce several anticancer bioactive compounds and is a source of lovastatin, which is used therapeutically to treat lipid disorders [21]. It may also cause aspergillosis [11]. *Aspergillus clavatus* (*A. clavatus*) is an allergenic species that causes hypersensitivity pneumonitis, also known as "malt workers' lung" [21]. *Aspergillus versicolor* (*A. versicolor*) is another common contaminant of damp buildings [8]. Finally, *A. nidulans* has been studied extensively since the 1940's as a scientific model organism [22]. It may also cause aspergillosis [11].

In the work described here, we investigate which species may successfully be identified through Raman spectroscopy using 785 nm excitation. In addition, in view of the medical and economic importance of these species, we make their averaged Raman spectra data freely available for download and use.

3.2. Materials and Methods

3.2.1. Sample Preparation

Strains used include *A. nidulans* (FGSC A4), *A. niger* (CBS 513.88), *A. flavus* (NRRL 3557), *A. fumigatus* (Af293), *A. oryzae* (ATCC 14895), *A. versicolor* (CBS 795.97), *A. clavatus* (NRRL1), *A. terreus* (NIH2624), *P. chrysogenum* (ATCC 10106), and *S. chartarum* (ATCC 201867). Strains were plated in triplicate onto minimal media (MM) [23] and incubated at 30 ˚C under continuous light. After 7 days, cultures were flooded with 2 mL sterile water and spores were dislodged by scraping with a sterile glass rod. The spore suspensions were then washed a minimum of three times each by

centrifuging for 1 min at 13000 rpm, as previously described [1]. Spore suspensions at a final concentration of 1×10^6 mL^{-1} were stored at 4 ˚C when not in use.

3.2.2. SERDS Experiments

The SERDS experimental setup is the same used for our previous work [2] (see Fig 2.1(a)). Briefly, ~ 6 μL of the spore suspension was deposited on a fused silica window (WG 41010, Thorlabs) and allowed to evaporate over the course of several hours, leaving the spores as a deposit on the surface. We then placed the sample under a Raman microscope (LabRAM HR Evolution, Horiba) for Raman interrogation using light emitted from a tunable laser working at ~ 785 nm, which was focused on the sample through a 100x objective (HCX PL Fluotar, N.A. 0.75). The backscattered signals from the sample were collected by the same objective. Two slightly different excitation wavelengths were applied to generate two spectra for each spore. Each recorded spectrum was the average of 12 5-second acquisitions, for a total integration time of 60 seconds. In general, each spectrum contains elements resulting from both Raman and fluorescence mechanisms. However, genuine Raman spectral features shift in unison with the excitation wavelength, while spectral features resulting from fluorescence mechanisms are independent of these shifts. The pure Raman spectrum can be retrieved by integrating the difference spectrum according to well-established SERDS protocols [24–30]. Here, post-processing of the raw data in order to retrieve the pure Raman spectra was similar to that described in our previous work [2].

3.2.3. Neural Network

In order to characterize the accuracy with which the raw and Raman spectra can be used to classify single spores as belonging to particular species, three neural network (NN) models were developed and tested using the TensorFlow software package [31]. Model 1 consisted of two sequential dense layers. The first layer was composed of 100 neurons activated by rectified linear unit (ReLU) functions. The output layer was composed of 8 neurons. Model 2 consisted of three sequential dense layers. The first two layers were composed of 100 neurons activated by ReLU functions. The output layer was composed of 8 neurons. Model 3 consisted in four sequential dense layers. The first three layers were composed of 100 neurons activated by ReLU functions. The output layer was composed of 8 neurons. All models were compiled using Adam optimization.

The data pool included the spectra from 100 spores each from *A. nidulans*, *A. flavus*, *A. oryzae*, *A. versicolor*, *A. fumigatus*, *A. niger*, *S. chartarum*, and *P. chrysogenum*, for a total of 800 spores. In order to evaluate the accuracy with which a single spore spectrum could be classified as belonging to one of the above eight species, the spectrum of each spore was in turn subtracted from the data pool while the remaining 799 spore spectra were used to train the NN. Evaluation of all 800 spores therefore required 800 separate instances of NN training with a corresponding 800 separate instances of applying the NN to the classification of a single spore spectrum. Each instance of training consisted of 20 epochs for which the order of the training spectra was randomly shuffled so as to reduce the dependence of the model on the sequence with which the data was measured.

The above protocol for training and classifying each of 800 spore spectra in turn was repeated 10 times to accumulate average statistics. Each NN model, therefore, was subjected to 8000 total instances of training and evaluation.

3.3. Results and Discussion

We report that, using a SERDS technique with an excitation wavelength of ~785 nm, conidia from neither *A. clavatus* nor *A. terreus* yielded a Raman signal of sufficient strength to be discernable above fluorescence. Fig 3.1 shows single spore Raman spectra of the species which yielded usable signals. The blue and purple curves correspond to Asymmetric Least-Squares (AsLS) [32] background-subtracted raw signals excited by two slightly different wavelengths. As can be seen, the genuine Raman features shift with excitation wavelength, while features resulting from fluorescence remain unaffected. The red curves correspond to the reconstructed, pure Raman spectra obtained through the SERDS protocol.

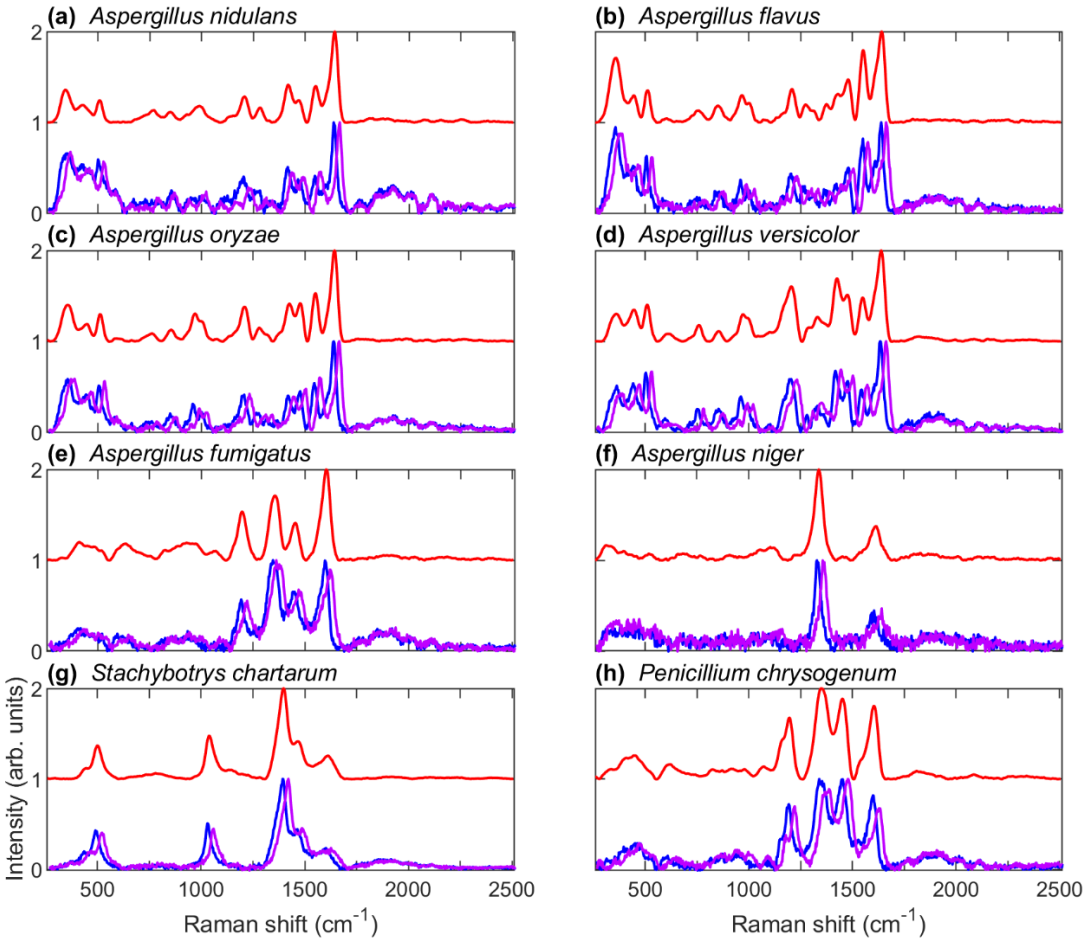

Figure 3.1. Single spore Raman spectra of species that yielded usable signals. The blue and purple curves correspond to Asymmetric Least-Squares (AsLS) [32] background-subtracted raw spectra excited by two slightly different frequencies, while the red curves correspond to the reconstructed, pure Raman spectra obtained through the SERDS protocol outlined in the S1 Appendix.

The region between approximately 1750 and 2500 cm^{-1} contains fine-scale fluorescence features common to all species. This is shown more fully in Fig 3.2. The curves are averages of AsLS [32] background-subtracted raw spectra obtained from multiple spores, corresponding to many different measurements of the blue curves shown in Fig 3.1. For *A. clavatus* and *A. terreus*, the number of different spores used was n = 50

and n = 10, respectively. For all other species, the number of different spores used was n = 100. In our previous work, we showed that for *A. nidulans* the Raman signal excited by a 785 nm laser originates in pigment molecules located within the cell wall [2]. Since the pool of species investigated here exhibits widely different melanin pigments, both the variety of major Raman features in Fig 3.1 and the similarity of the fine-scale fluorescence features in Fig 3.2 support the hypothesis that at 785 nm the Raman signal originates in melanin pigments within the cell wall while the fine-scale fluorescence signal originates from constituents of the cell wall itself, regardless of species. In fungi, the cell wall is composed of a highly cross-linked biopolymer formed from glucans, chitin and chitosan, mannans and/or galactomannans, and glycoproteins [33]. Further investigation is required to determine which of these molecular constituents is responsible for the fine-scale fluorescence features shown in Fig 3.2. It should be noted that *S. chartarum* does not exhibit these fine-scale fluorescence features or, if it does, exhibits them only weakly. Of the species investigated, *S. chartarum* is the only one which produces conidial spores covered in a layer of slime, which may possibly serve to suppress the mechanism responsible for the fine-scale fluorescence exhibited in other species. We have hypothesized elsewhere [2] that the fine-scale fluorescence features may be facilitated by the formation of long-lived molecular cages within the biopolymer of the cell wall, thus partially shielding fluorophores from the substantial inhomogeneous broadening they would otherwise experience in a different environment [34, 35].

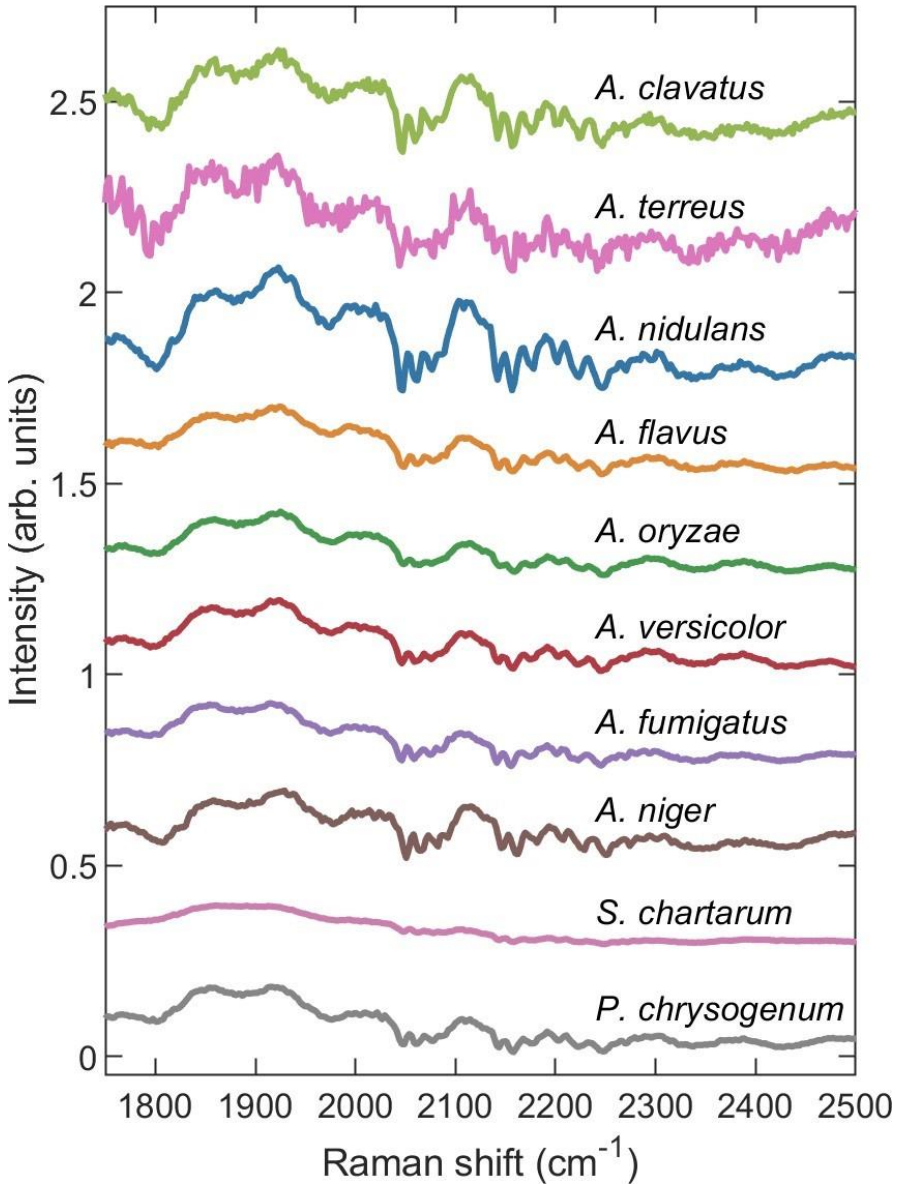

Figure 3.2. Averaged AsLS background-subtracted raw spectra showing fine-scale fluorescence features in the range ~1750 to 2500 cm^{-1}.

The hypothesis that the Raman signal originates in melanin pigments within the cell wall is further supported through an investigation of the melanin biosynthesis pathway of each species. Fungal melanins are negatively charged, hydrophobic, and of high molecular weight. Melanin functions to protect the fungal microorganism from harmful

environmental conditions such as ultraviolet light-induced and oxidant-mediated damages, temperature extremes, hydrolytic enzymes, heavy metal toxicity, and anti-microbial drugs [36]. In conidial spores, they are concentrated and bound within the cell wall. Because of their integration within the cross-linked network that constitutes the cell wall, the molecular structures of fungal melanins remain notoriously recalcitrant to characterization [36, 37]. Nevertheless, two main pathways for fungal melanin biosynthesis have been identified. One pathway begins with malonyl-CoA and leads to the polymerization of 1,8-dihydroxynapthalene (DHN), resulting in DHN-melanin. An alternative pathway begins with L-dopa or tyrosine and leads to polymerization of dihydroxyindoles, resulting in DOPA-melanin [36].

To our knowledge, the melanin biosynthesis pathways of only six of the ten species under investigation have been studied. *A. terreus* possesses a DHN-melanin pathway [38], as does *A. fumigatus* [39, 40]. The biosynthesis pathway classifications of the fungi *A. nidulans*, *A. oryzae*, *A. flavus*, and *A. niger* remain uncertain [37]. It has long been recognized that these species possess gene orthologues encoding Polyketide Synthases (PKSs) that in *A. fumigatus* are responsible for the production of DHN melanin. However, their role in conidial pigmentation for *A. niger* and *A. flavus* is doubtful [37]. *A. nidulans*, *A. oryzae*, *A. flavus*, and *A. niger* have all at one time been classified as DOPA melanin producers [38, 40, 41]. In *A. oryzae*, culturing in the presence of the DOPA precursor tyrosine results in the production of DOPA melanin [42]. DOPA pathway inhibitors have prevented pigmentation in *A. nidulans* [41], *A. flavus* [38], and *A. niger* [38], although subsequent work seemed to cast doubt on these results [43]. It has been surmised that the

black pigment of *A. niger*, known as aspergillin, is actually a polymerization of two different pigments, one brown and one green. Consequently, the pigmentation of *A. niger* is acknowledged to be complex and is still under investigation [37]. Regardless, what is abundantly clear from the literature is that *A. nidulans*, *A. flavus*, and *A. niger* do not respond to DHN pathway inhibitors [38, 41, 43].

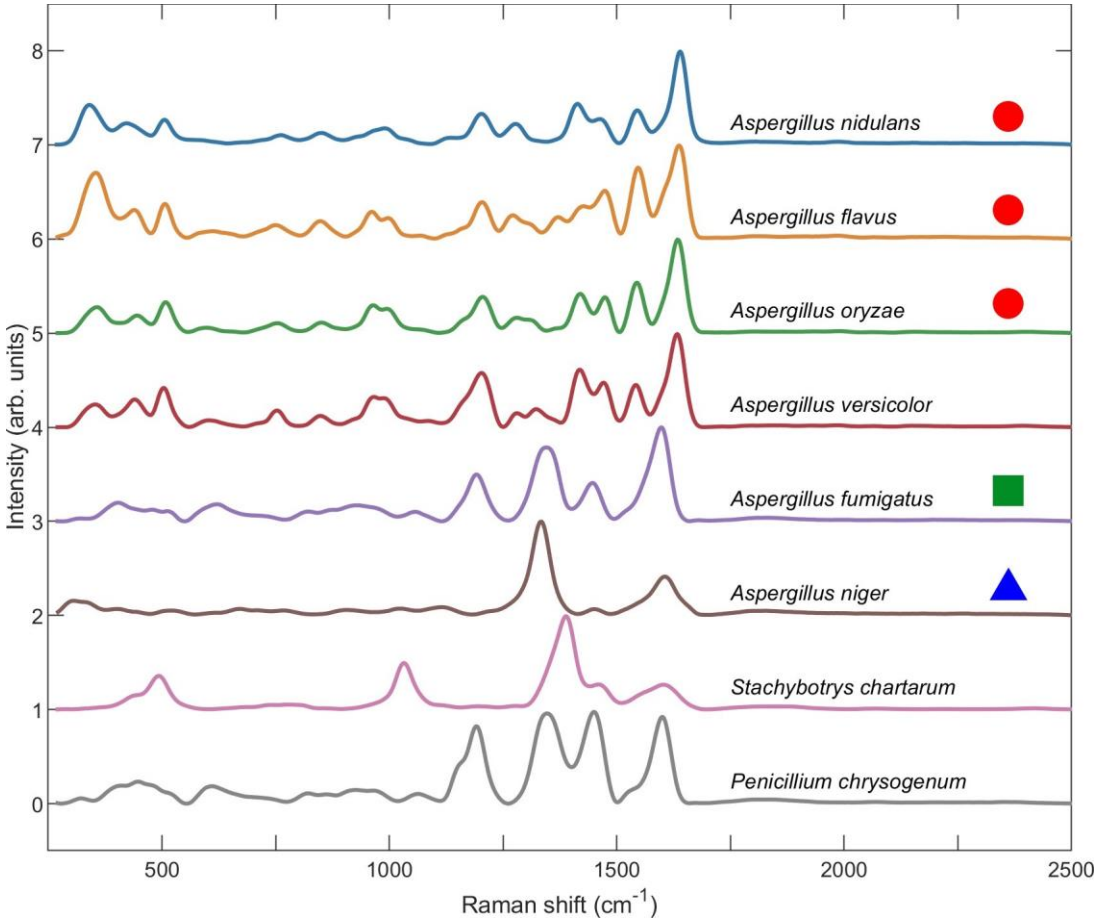

Figure 3.3. Pure Raman spectra of various species retrieved from the SERDS protocol. Each spectrum is the average of the SERDS spectra retrieved from n = 100 individual spores. The red circles indicate that a species either produces DOPA melanin when cultured in the presence of tyrosine (*A. oryzae*) or remains unaffected by DHN pathway inhibitors (*A. nidulans* and *A. flavus*). The green square indicates that conidial pigmentation is due to DHN melanin (*A. fumigatus*). The blue triangle indicates that, while *A. niger* is not affected by DHN pathway inhibitors, it is thought to polymerize two pigments [37, 38].

It can be seen in Fig 3.3 that the melanin biosynthesis pathway of a species correlates with major features in its reconstructed, pure Raman spectrum. The top four spectra are remarkably similar. As stated above, three of these species have been shown either to produce DOPA melanin when cultured in the presence of tyrosine (*A. oryzae*) or remain unaffected by DHN pathway inhibitors (*A. nidulans* and *A. flavus*). It is therefore likely that *A. versicolor* is not affected by DHN pathway inhibitors, as well, although to our knowledge no study on the melanin biosynthesis pathway of this species has been completed. It can also be seen that, although *A. niger* also remains unaffected by DHN pathway inhibitors, the unusual complexity of its pigmentation is fully reflected in the vast difference of its Raman spectrum from the other Aspergillus species. We point out that *A. fumigatus*, whose conidial pigmentation is produced through the DHN pathway, exhibits a different Raman spectrum from the rest of the Aspergillus species. The similarity between the Raman spectra of *A. fumigatus* and *P. chrysogenum* leads us to suppose that DHN pathway inhibitors will be able to prevent pigmentation in *P. chrysogenum*, although to our knowledge the melanin biosynthesis pathway of this species has not been studied. Neither has the melanin biosynthesis pathway of *S. chartarum* been studied, but its Raman spectrum suggests that possibly, like *A. niger*, its biosynthesis pathway may be more complex than other species. Even the spectra of *A. terreus*, which did not yield a Raman signal of sufficient strength to be reliably measured, fits into this paradigm. *A. terreus* is unique among Aspergilli in that it does not use the commonly found Polyketide Synthases (PKSs) for pigment biosynthesis, as do other Aspergillus species. Instead, *A. terreus* pigment biosynthesis occurs through enzymes similar to NonRibosomal-Peptide

Synthetases (NRPSs), namely MelA, the only such enzymes found thus far [37, 44]. Unfortunately, the literature contains little information on melanin biosynthesis pathway for *A. clavatus*.

The fact that a species' melanin biosynthesis pathway correlates with major features in its Raman spectrum is perhaps not surprising, given the above evidence that the Raman signal originates from melanin within the cell wall. Similar melanin biosynthesis pathways begin and end with similar molecules, each possessing similar vibrational modes which, upon optical excitation, result in similar Raman spectra. The minor differences in the location and amplitude of various peaks in these Raman spectra may be reflective of differences in (1) the structure of molecular precursors, (2) the polymerization enzymes responsible for melanin production, (3) and/or the ratios of molecular components of the cell wall into which the pigments have been integrated. The remarkable similarity between the Raman spectra of some of the species under investigation begs the question of whether their Raman spectra may be used to successfully identify and differentiate them. It is to this question that we now turn to next.

Neural Networks (NN) are powerful tools for the analysis of multidimensional data [45, 46]. Indeed, they are often able to distinguish data patterns that remain invisible to unaided human perception. Consequently, they are increasingly being used across many fields, including cancer diagnosis [47, 48], communications [49], cyber security [50], earthquake detection and location [51], and construction automation [52]. Here, we use a NN model to assess the accuracy with which a spectrum from a single spore may be used to classify the species to which that spore belongs. We point out that our goal is not the

development of an optimized model, but rather the characterization of a baseline model from which further improvements can be made.

We tested three different NN models of increasing complexity as outlined in **Materials and Methods**, consisting of two, three, and four sequential layers, respectively. Two different types of spectra were used for single spore species characterization: (1) the pure Raman spectrum retrieved through the SERDS protocol and (2) the AsLS background-subtracted raw spectrum. These spectra types correspond to the red and blue curves shown in Fig 3.1, respectively. The NN classification accuracy for spores of eight different species is listed in Table 3.1. We point out that in all cases the classification accuracy never drops below 99%. If significance is attached to the approximately 1% error, it can be seen that *A. versicolor* poses the greatest challenge to classification, since it can exhibit a widely varying spore color. In addition, it can be seen that in all cases the raw spectrum exhibits greater total classification accuracy than the pure Raman spectrum. This may be due to an amount of spectral information contained in the fluorescence response that is excluded from the pure Raman signal. Finally, as the NN model complexity increases with the number of layers, the classification accuracy of the raw spectrum decreases, which is indicative of overfitting. Consequently, the greatest total classification accuracy of 99.975% is achieved with a simple two-layer NN model using raw measured spectra. Regardless, it is evident that remarkable classification accuracy can be achieved even for species that exhibit spectra as similar as those shown in Fig 3.3.

Table 3.1. Percent accuracy with which single spore spectra from a given species may be classified using the Neural Network (NN) models described in methods and materials.

Model	*Layers*	*Measurement*	*A. nidulans*	*A. flavus*	*A. oryzae*	*A. versicolor*	*A. fumigatus*	*A. niger*	*S. chartarum*	*P. chrysogenum*	*Total*
1	2	Raman	100	100	100	99.7	100	100	100	99.2	99.8625
		Raw	100	100	100	99.8	100	100	100	100	99.975
2	3	Raman	100	100	100	99.9	100	100	100	99.6	99.9375
		Raw	100	100	100	99.6	100	100	100	100	99.95
3	4	Raman	100	100	99.9	99.6	100	100	100	99.7	99.9
		Raw	99.9	100	100	99.7	99.9	100	100	100	99.9375

3.4. Conclusion

We have used a 785 nm SERDS technique to measure the Raman spectra of single conidial spores of 10 mold species of especial toxicological, medical, and industrial importance. In conjunction with our previous work [2], both the pure Raman and fluorescence signals support the hypothesis that the Raman signal originates from the melanin pigments bound within the highly cross-linked cell wall of the conidium. The major features of the Raman spectrum correlate with the melanin bio-synthesis pathway: species that either produce DOPA melanin when cultured in the presence of tyrosine or remain unaffected by DHN pathway inhibitors exhibit similar Raman spectra, which differ in turn from the Raman spectra of species that produce DHN melanin. Species with a complex melanin bio-synthesis pathway exhibit even more varying Raman spectra. These Raman spectral relationships lead us to predict that *A. versicolor* will not be affected by DHN pathway inhibitors, while in *P. chrysogenum* DHN pathway inhibitors may prevent conidial pigmentation. In the future we expect that Raman spectroscopy will become a powerful tool in the characterization of fungal melanins and their biosynthetic pathways when used in conjunction with genetic and chemical inhibitor approaches. Recently

Pacelli *et al*. [53] demonstrated through a multidisciplinary approach that the fungus *Cryomyces antarcticus* produces both DHN and DOPA melanin in differing amounts. It is possible that the same may be true of other species, as well. Our work demonstrates that Raman spectroscopy can be used in such a multidisciplinary approach to great effect.

We highlight the fact that two of the investigated species, *A. terreus* and *A. clavatus*, did not exhibit Raman spectra that could be measured reliably over against the fluorescence response. As noted above, this is likely due to the characteristics of the melanin molecules within the cell wall. In the case of *A. terreus*, its unique biosynthesis pathway makes it an exception among mold species. The melanin biosynthesis pathway of *A. clavatus*, to our knowledge, remains unknown. Regardless, these facts must be taken into account in the design of a system for Raman identification of mold species. While spontaneous Raman techniques offer simplicity of implementation, a more complex coherent Raman characterization technique, such as CARS [1], may be able to successfully measure a Raman spectrum where a spontaneous Raman technique fails, since coherent Raman processes give a much larger signal. The pros and cons of each approach must be weighed.

In addition, we found that for those species which exhibited measurable Raman spectra, a species classification accuracy above 99% was easily achieved with simple NN models. This is highly encouraging and bodes well for the success of Raman identification of mold species, even for those species whose Raman spectra exhibit a high degree of similarity. Moreover, the implementation of a fluorescence-suppression technique, in this case SERDS, is not necessary for successful and highly accurate species classification,

since our results indicate that the presence of fine-scale fluorescence features in the spectrum does not detract from the information contained in the Raman response. Raw measured spectra even exhibited a slightly greater classification accuracy than those spectra calculated through a SERDS protocol, due to minor variations in the fluorescence response that aid in classification. Consequently, while fluorescence suppression techniques are required in order to retrieve an accurate Raman spectrum, for identification purposes alone a simple "point and shoot" technique will still be highly accurate.

The above results demonstrate the practicality of Raman spectroscopy for the identification of toxic and industrial mold species. Full implementation, however, depends on the development of a mobile Raman microspectrometer. Current commercial handheld spectrometers will not suffice, since analysis of mold conidia requires sensitive control of sample position, laser power, and spectral integration settings, all of which these devices do not offer. Commercial Raman microspectrometers, however, which do offer sufficient experimental finesse for the application, are bulky and cannot easily be transported. Portability would require miniaturization, and such a product does not currently exist on the market. Nevertheless, the main components of a portable Raman microspectrometer, namely (1) a miniaturized intensified CCD spectrometer, (2) a compact variable-power Raman laser source, and (3) a finely-tuned microscope stage, all exist commercially as independent products. What remains to be done is only a matter of assembling them into an integrated device, which we intend to accomplish in our future research.

Finally, we wish to emphasize that this is the first time the Raman spectra of the toxic *S. chartarum* and infectious *A. fumigatus* have been published. We have also

measured the Raman spectra of the carcinogenic *A. flavus*, medicinal *P. chrysogenum*, and industrial *A. oryzae* and *A. niger*. Other important species are included, as well. Both the pure Raman and raw spectra of all these species are made freely available for download and use online [54].

3.5. References

[1] Strycker BD, Han Z, Commer B, Shaw BD, Sokolov AV, Scully MO. CARS spectroscopy of Aspergillus nidulans spores. Sci Rep. 2019; 9: 1789.

[2] Han Z, Strycker BD, Commer B, Wang K, Shaw BD, Scully MO, et al. Molecular origin of the Raman signal from Aspergillus nidulans conidia and observation of fluorescence vibrational structure at room temperature. Sci Rep. 2020; 10: 5428.

[3] Butler HJ, Ashton L, Bird B, Cinque G, Curtis K, Dorney J, et al. Using Raman spectroscopy to characterize biological materials. Nat Protoc. 2016; 11(4):664–87.

[4] Ghosal S, Macher JM, Ahmed K. Raman microspectroscopy-based identification of individual fungal spores as potential indicators of indoor contamination and moisture-related building damage. Environ Sci Technol. 2012; 46(11):6088–95.

[5] Farazkhorasani F. Raman and SERS studies of filamentous fungi [Masters Thesis]. [Winnipeg, Canada]: University of Manitoba; 2014.

[6] Kuhn DM, Ghannoum MA. Indoor mold, toxigenic fungi, and Stachybotrys chartarum: infectious disease perspective. Clin Microbiol Rev. 2003; 16(1):144–72.

[7] Forgacs J. Stachybotryotoxicosis. In: Microbial Toxins. Academic Press; 1972. p. 95–128.

[8] Gravesen S, Nielsen PA, Iversen R, Nielsen KF. Microfungal contamination of damp buildings—examples of risk constructions and risk materials. Environ Health Perspect. 1999; 107: 505–8.

[9] Najafpour GD. Biochemical Engineering and Biotechnology. Elsevier; 2007.

[10] de Vries RP, et al. Comparative genomics reveals high biological diversity and specific adaptations in the industrially and medically important fungal genus Aspergillus. Genome Biol. 2017; 18: 28.

[11] Latge JP. Aspergillus fumigatus and aspergillosis. Clin Microbiol Rev. 1999; 12(2):310–50.

[12] Wilson BJ. Miscellaneous Aspergillus toxins. In: Microbial Toxins. Academic Press; 1971. p. 207–95.

[13] Fungal infections, Aspergillus fumigatus [Internet]. Leading International Fungal Education. [cited 2020 Jul 23]. Available from: http://www.life-worldwide.org/fungal-diseases/aspergillus-fumigatus

[14] Nierman WC, Nelson KE. Genomics for applied microbiology. Adv Appl Microbiol. 2002; 51: 201–45, 246e–8e.

[15] Ahmed ME. Extraction and purification of protease from Aspergillus niger isolation. Pharm Pharmacol Int J. 2018; 6(2): 96–9.

[16] Fungal infections, Aspergillus niger [Internet]. Leading International Fungal Education. [cited 2020 Jul 23]. Available from: http://www.life-worldwide.org/fungal-diseases/aspergillus-niger

[17] Hesseltine CW. A millennium of fungi, food, and fermentation. Mycologia. 1965; 57(2):149–97.

[18] Gomi K. Aspergillus oryzae. In: Encyclopedia of Food Microbiology. Academic Press; 2000. p. 66–71.

[19] Bhatnagar D, Cleveland TE, Payne GA. Aspergillus flavus. In: Encyclopedia of Food Microbiology. Academic Press; 2000. p. 72–9.

[20] Klich MA. Aspergillus flavus: the major producer of aflatoxin. Mol Plant Pathol. 2007; 8(6):713–22.

[21] Nadumane VK, Venkatachalam P, Gajaraj B. Aspergillus Applications in Cancer Research. In: New and Future Developments in Microbial Biotechnology and Bioengineering: Aspergillus System Properties and Applications. Elsevier; 2016. p. 243–55.

[22] Gavrias V, Timberlake WE, Adams TH. Aspergillus nidulans. In: Encyclopedia of Genetics. Academic Press; 2001. p. 106–11.

[23] Hill TW, Kafer E. Improved protocols for Aspergillus minimal medium: trace element and minimal medium salt stock solutions. Fungal Genet Rep. 2001; 48(8).

[24] Shreve AP, Cherepy NJ, Mathies RA. Effective rejection of fluorescence interference in Raman spectroscopy using a shifted excitation difference technique. Appl Spectrosc. 1992; 46(4):707–11.

[25] Zhao J, Carrabba MM, Allen FS. Automated fluorescence rejection using shifted excitation Raman difference spectroscopy. Appl Spectrosc. 2002; 56(7):834–45.

[26] Sowoidnich K, Kronfeldt H-D. Shifted excitation difference spectroscopy at multiple wavelengths for insitu meat species differentiation. Appl Phys B. 2012; 108(4):975–82.

[27] da Silva Martins MA, Ribeiro DG, dos Santos EAP, Martin AA, Fontes A, da Silva Martinho H. Shiftedexcitation Raman difference spectroscopy for in vitro and in vivo biological samples analysis. Biomed Opt Express. 2010; 1(2):617–26.

[28] Matousek P, Towrie M, Parker AW. Simple reconstruction algorithm for shifted excitation Raman difference spectroscopy. Appl Spectrosc. 2005; 59(6):848–51.

[29] Oshima Y, Komachi Y, Furihata C, Tashiro H, Sato H. Fluorescence-suppressed Raman technique for quantitative analysis of protein solution using a micro-Raman probe, the shifted excitation method. Appl Spectrosc. 2006; 60(9):964–70.

[30] Gebrekidan MT, Knipfer C, Stelzle F, Popp J, Will S, Braeuer A. A shifted-excitation Raman difference spectroscopy (SERDS) evaluation strategy for the efficient isolation of Raman spectra from extreme fluorescence interference. J Raman Spectrosc. 2016; 47(2):198–209.

[31] Abadi M, Agarwal A, Barham P, Brevdo E, Chen Z, Citro C, et al. TensorFlow: Large-scale machine learning on heterogeneous systems [Internet]. 2015. Available from: tensorflow.org

[32] Eilers PH, Boelens HF. Baseline correction with asymmetric least squares smoothing. Leiden Univ Med Cent Rep. 2005; 1:5.

[33] Free SJ. Fungal cell wall organization and biosynthesis. In: Advances in Genetics. Elsevier; 2013. p.33–82.

[34] Cicogna F, Coiai S, Pinzino C, Ciardelli F, Passaglia E. Fluorescent polyolefins by free radical postreactor modification with functional nitroxides. React Funct Polym. 2012; 72: 695–702.

[35] Prampolini G, Monti S, De Mitri N, Barone V. Evidences of long lived cages in functionalized polymers: effects on chromophore dynamic and spectroscopic properties. Chem Phys Lett. 2014; 601: 134–8.

[36] Pombeiro-Sponchiado SR, Sousa GS, Andrade JCR, Lisboa HF, Goncalves RCR. Production of melanin pigment by fungi and its biotechnological applications. In: Melanin. IntechOpen; 2017. p. 47–75.

[37] Chang PK, Cary JW, Lebar MD. Biosynthesis of conidial and sclerotial pigments in Aspergillus species. Appl Microbiol Biotechnol. 2020; 104: 2277–86.

[38] Pal AK, Gajjar DU, Vasavada AR. DOPA and DHN pathway orchestrate melanin synthesis in Aspergillus species. Med Mycol. 2014; 52(1):10–8.

[39] Bayry J, Beaussart A, Dufrene YF, Sharma M, Bansal K, Kniemeyer O, et al. Surface structure characterization of Aspergillus fumigatus conidia mutated in the melanin synthesis pathway and their human cellular immune response. Infect Immun. 2014; 82(8):3141–53.

[40] Langfelder K, Streibel M, Jahn B, Haase G, Brakhage AA. Biosynthesis of fungal melanins and their importance for human pathogenic fungi. Fungal Genet Biol. 2003; 38(2):143–58.

[41] Goncalves RC, Lisboa HC, Pombeiro-Sponchiado SR. Characterization of melanin pigment produced by Aspergillus nidulans. World J Microbiol Biotechnol. 2011; 28(4):1467–74.

[42] Haneda K, Watanabe S, Takeda I. Synthesis of L-3,4-dihydroxyphenylalanine from L-tyrosine by microorganisms. Appl Microbiol. 1971; 22(4):721–2.

[43] Chang PK, Scharfenstein LL, Mack B, Wei Q, Gilbert M, Lebar M, et al. Identification of a copper-transporting ATPase involved in biosynthesis of A. flavus conidial pigment. Appl Microbiol Biotechnol. 2019; 103: 4889–97.

[44] Geib E, Gressler M, Viediernikova I, Hillmann F, Jacobsen ID, Nietzsche S, et al. A non-canonical melanin biosynthesis pathway protects Aspergillus terreus conidia from environmental stress. Cell Chem Biol. 2016; 23: 587–97.

[45] Haykin S. Neural Networks: A Comprehensive Foundation. Macmillan Coll Div; 1994.

[46] Aggarwal CC. Neural Networks and Deep Learning. Springer; 2018.

[47] Yu KH, Zhang C, Berry GJ, Altman RB, Re C, Rubin DL, et al. Predicting non-small cell lung cancer prognosis by fully automated microscopic pathology image features. Nat Commun. 2016; 7: 12474.

[48] McKinney SM, Sieniek M, Godbole V, Godwin J, Antropova N, Ashrafian H, et al. International evaluation of an AI system for breast cancer screening. Nature. 2020; 577: 89–94.

[49] Farsad N, Goldsmith A. Neural network detection of data sequences in communication systems. IEEE Trans Signal Process. 2018; 66(21):5663–78.

[50] Vinayakumar R, Soman KP, Poornachandran P. Applying convolutional neural network for network intrusion detection. In Udupi; 2017. p. 1222–8.

[51] Perol T, Gharbi M, Denolle M. Convolutional neural network for earthquake detection and location. Sci Adv. 2018; 4(2): e1700578.

[52] Dung CV, Anh LD. Autonomous concrete crack detection using deep fully convolutional neural network. Autom Constr. 2019; 99: 52–8.

[53] Pacelli C, Cassaro A, Maturilli A, Timperio AM, Gevi F, Cavalazzi B, et al. Multidisciplinary characterization of melanin pigments from the black fungus Cryomyces antarcticus. Appl Microbiol Biotechnol. 2020; 104: 6385–95.

[54] Strycker B, Han Z, Duan Z, Commer B, Wang K, Shaw B, et al. Identification of toxic mold species through Raman spectroscopy of fungal conidia. Open Sci Framew [Internet]. 2020 Oct 20; Available from: https://doi.org/10.17605/OSF.IO/X6T5W

4. RAMAN CHARACTERIZATION OF FUNGAL DHN AND DOPA MELANIN BIOSYNTHESIS PATHWAYS*

Fungal melanin represents a resource for important breakthroughs in industry and medicine, but the characterization of their composition, synthesis, and structure is not well understood. Raman spectroscopy is a powerful tool for the elucidation of molecular composition and structure. In this work, we characterize the Raman spectra of wild-type *Aspergillus fumigatus* (*A. fumigatus*) and *Cryptococcus neoformans* (*C. neoformans*) and their melanin biosynthetic mutants and provide a rough "map" of the DHN (*A. fumigatus*) and DOPA (*C. neoformans*) melanin biosynthetic pathways. We compare this map to the Raman spectral data of *Aspergillus nidulans* (*A. nidulans*) wild-type and melanin biosynthetic mutants obtained from a previous study. We find that the fully polymerized *A. nidulans* melanin cannot be classified according to the DOPA pathway; nor can it be solely classified according to the DHN pathway, consistent with mutational analysis and chemical inhibition studies. Our approach points the way forward for an increased understanding of, and methodology for, investigating fungal melanins.

4.1. Introduction

The difficulty of characterizing melanin, including fungal melanin, has long been recognized. Fungal melanin is negatively charged, hydrophobic, of high molecular weight, highly heterogeneous, insoluble in organic solvents, and resistant to chemical degradation [1,2]. Melanin is concentrated in the cell wall and bound within the cross-linked network

that composes it, making elucidation of the melanin molecular structure notoriously recalcitrant to characterization [1,3]. Nevertheless, two main pathways for fungal melanin biosynthesis have been identified. One pathway begins with malonyl-CoA and leads to the polymerization of 1,8-dihydroxynapthalene (DHN), resulting in DHN-melanin. An alternative pathway begins with L-dopamine or tyrosine and leads to polymerization of dihydroxyindoles, resulting in DOPA-melanin [1]. The model organisms for the DHN and DOPA melanin biosynthesis pathways are *A. fumigatus* (Figure 4.1(a)) and *C. neoformans* (Figure 4.1(c)), respectively.

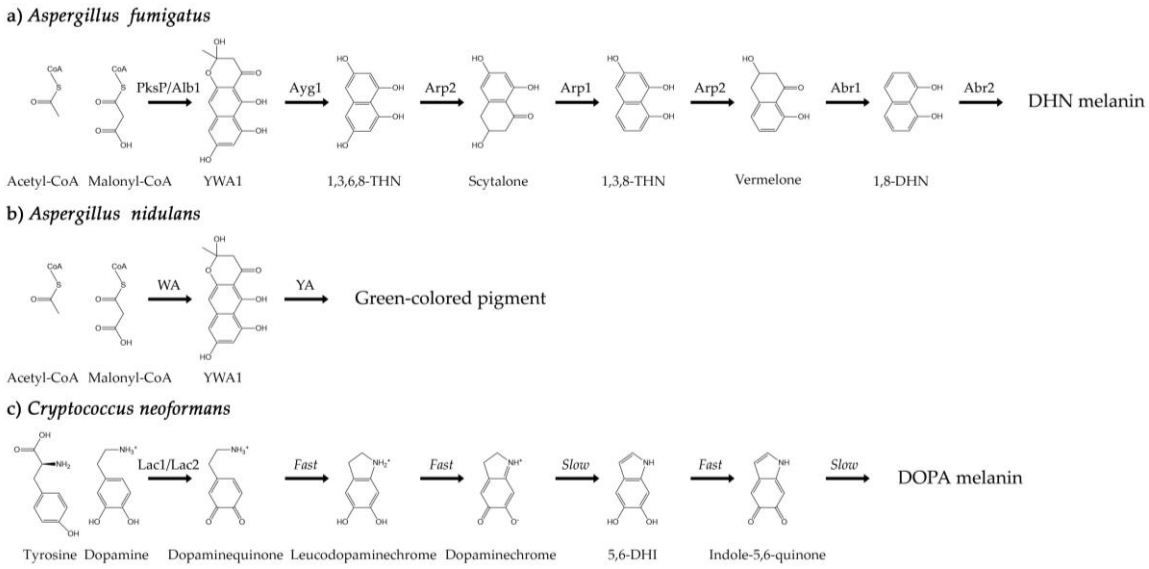

Figure 4.1. (a) The biosynthesis pathway of DHN melanin in *A. fumigatus* conidia. Acetyl- and malonyl-CoA are converted through a series of reactions catalyzed by six different enzymes. (b) The biosynthesis pathway of the green-colored pigment in *A. nidulans* conidia. Acetyl- and malonyl-CoA are converted through a series of reactions involving the WA and YA enzymes. The final product has not yet been fully characterized. (c) The biosynthesis pathway of DOPA melanin in *C. neoformans* cells. The initial conversion of tyrosine or dopamine to dopaminequinone is catalyzed primarily by the Lac1 enzyme. Subsequent reactions occur through a Raper–Mason scheme.

A. fumigatus is an opportunistic ascomycete filamentous pathogen whose airborne conidia are among the most prevalent worldwide. This fungus is responsible for 90% of aspergillosis cases, the life-threatening infection of the lungs in immunocompromised individuals [4–6]. Notably, the polyketide-derived DHN melanin that *A. fumigatus* synthesizes plays a key role in its virulence [7,8]. Biosynthesis of this melanin during conidiation involves six enzymes encoded by a gene cluster located on the second chromosome [9,10]. The melanin is synthesized de novo endogenously in endosomes and subsequently secreted for incorporation into the cell wall [11–13], anchored mostly by chitin [7].

C. neoformans is an opportunistic basidiomycete yeast responsible for the vast majority of fungal meningoencephalitis cases worldwide [14,15]. It enters the lungs through inhalation of spores or desiccated yeasts and, in immunocompromised individuals, often disseminates to the brain. If left untreated, the infection is lethal [14,15]. The virulence of *C. neoformans* is enhanced through both the growth of a polysaccharide capsule and melanization [16–18]. Unlike *A. fumigatus*, *C. neoformans* requires an exogeneous substrate such as L-dopamine or tyrosine to synthesize DOPA melanin [16]. The biosynthesis of this melanin is primarily catalyzed by a laccase enzyme encoded by *LAC1* first [19], and subsequent reactions occur through a Raper–Mason scheme [19–24]. Acid hydrolysis of melanized *C. neoformans* cells results in spherical hollow shells, called "ghosts," composed almost entirely of melanin [25]. The same may be done with *A. fumigatus* conidia [13].

The melanin biosynthesis pathways of almost all fungi are thought to fall within the paradigms exemplified by *A. fumigatus* and *C. neoformans*. However, uncertainty about a given fungus' melanin biosynthetic pathway can persist in the literature for years. For example, early studies in 1969 [26] and 1970 [27] indicated that the model filamentous fungus *A. nidulans*, which is closely related to the DHN-producing *A. fumigatus*, contained DOPA melanin in mycelia. Goncalves et al., concluded the same in 2012 using the melaninoverproducing mutants *mel1* and *mel2*, which exhibit brown pigmentation in mycelia [28]. In regard to conidial pigmentation, however, studies in 1999 [29] and 2001 [30] showed that the *wA* gene common to both *A. nidulans* and *A. fumigatus* encodes a polyketide synthase that can generate the naphthopyrone compound YWA1, the first precursor for conidial melanin formation in both species. Subsequent steps in conidial melanin formation for *A. nidulans* are less clear, especially when the results of chemical inhibition of biosynthesis are considered. Wheeler and Bell showed in 1988 that *A. nidulans* is unaffected by the chemical biosynthesis inhibitor tricyclazole, which inhibits conidial DHN melanin production in other species, like *A. fumigatus* [31]. Whole genome sequences show that *A. nidulans* does not carry the targeted reductases like Arp2 in the DHN melanin biosynthetic pathway [30]. It is known that the conidial melanin biosynthesis pathway of *A. nidulans* involves two genes, *wA* and *yA*, that encode the polyketide synthase WA and the laccase YA, respectively, which result in a green conidial pigment of unknown composition and structure (Figure 4.1(b)) [32]. Indeed, the uncertainty in regard to the conidial melanin of *A. nidulans* is such that, as late as 2020, it

has been observed that “the involvement of the DOPA-melanin pathway in the formation of conidial pigment of this Aspergillus model species is still an open question” [3].

In the present work, we find that the fully polymerized *A. nidulans* melanin can be neither classified according to the DOPA pathway nor solely classified according to the DHN pathway, consistent with mutational analysis and chemical inhibition. We developed a multi-disciplinary method that takes advantage of the accumulation of melanin precursor molecules in pigment mutants of a target species and preferentially selects these melanin precursor molecules for Raman spectral measurement in vivo, thus providing a spectral “fingerprint” of each melanin precursor that can be used for further analysis and comparison [33,34]. The preferential selection of the melanin precursor molecules occurs through a resonant Raman process [35] excited by approximately 785 nm, while fluorescence signals that would otherwise disguise the information contained in the Raman spectrum are excluded through use of a Shifted Excitation Raman Difference (SERDS) technique (see [33,34] and references therein). Our spectroscopic technique has several advantages over conventional infrared spectroscopy of fungal melanin [36]: (1) It requires no sample preparation. That is, no extraction of the melanin from the cell wall matrix is required, thus preserving its native composition and structure. (2) It is insensitive to water absorption in the cells. Additionally, unlike typical infrared techniques, (3) it can preferentially select the melanin precursor molecules for analysis through a resonant physical mechanism.

Since the Raman spectrum of a given molecule is indicative of its structure, melanin precursor molecules that have similar Raman spectra also have similar chemical

structures. Thus, by measuring the Raman spectra of the melanin precursors contained in the pigment mutants of *A. fumigatus* and *C. neoformans*, a rough but nevertheless accurate "map" of the biosynthesis pathways of each organism can be constructed, which may be used to compare with other species. Here, we complete this "map," and use it to elucidate the nature of melanin biosynthesis in *A. nidulans* conidia. We show that the DOPA pathway has no bearing on the production of melanin in *A. nidulans* conidia. Furthermore, while the conidial pigment produced by *A. nidulans* begins with the polyketide synthase, the final product diverges from a dichotomous classification scheme (either DOPA or DHN). Our current data are consistent with previous genetic characterization and support a new classification of melanin produced by *A. nidulans*. We show that more exact terminology is needed, especially since "research on chemical structures and biosynthetic pathways of conidial and sclerotial pigments in aspergilli is still at its infancy" [3].

We anticipate that the technique outlined below will become a powerful tool in the characterization of fungal melanin, which are attractive as low-cost and high-yield alternatives to synthetic, animal, and plant melanin [37], and have great potential for powerful and eco-friendly breakthroughs in industry and medicine.

4.2. Materials and Methods

4.2.1. Phenotypic Assay

A. fumigatus strains (wild type B5233 and melanin mutant *alb1*Δ, *ayg1*Δ, *arp1*Δ, *arp2*Δ, *abr1*Δ, *abr2*Δ [9]) from −80 ˚C glycerol stocks were streaked onto standard Aspergillus solidified complete media (CM). Cells were then cultured at 30 ˚C for 3 days. *A. fumigatus* mutants and wild-type spores were collected in 1 × PBS + 0.2% Tween-20.

Spores were counted using a hemocytometer and diluted to a final concentration of 2 × 10^6 cells/mL. A total of 10 µL of the spore suspension was spread onto CM plates and incubated at 30 ˚C. At day 2 and day 3, spores were collected and fixed in 3.7% formaldehyde. Images were acquired on day 2 and day 3 (Figure 4.2(a)).

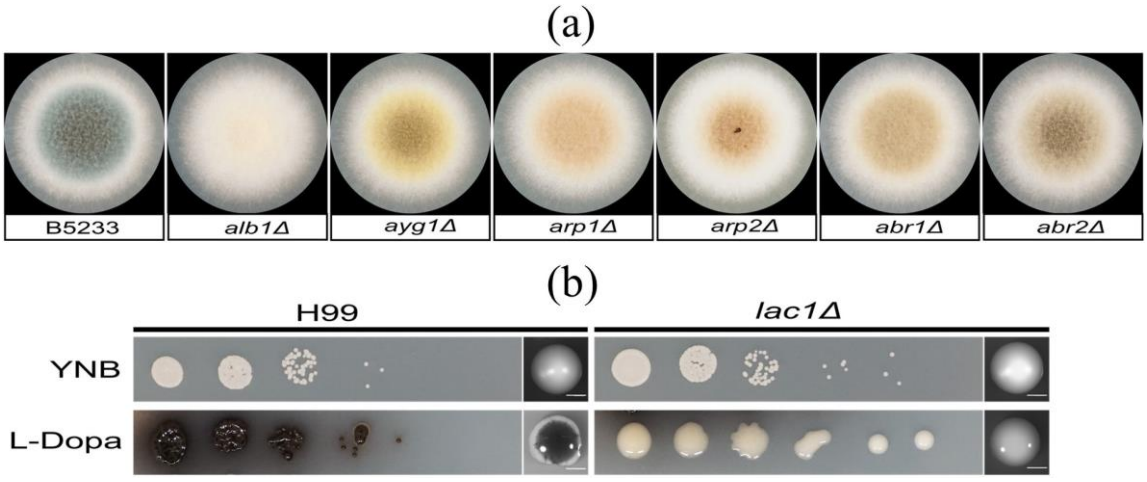

Figure 4.2. (a) Individual colony of the melanin mutant and the *A. fumigatus* wild-type control (B5233). A total of 10 µL of a 2 × 10^6 cells/mL cell suspension for each strain was inoculated onto the center of an *Aspergillus* complete media (CM) plate. The plates were incubated at 30 ˚C for 3 days. (b) The laccase mutant (*lac1*Δ) and the *C. neoformans* wild-type control (H99). In total, 3 µL of the serial dilutions were dropped onto YNB medium and L-Dopa media. Scale bar: 2000 µm.

C. neoformans strains (wild type H99 and lac1Δ [23]) from −80 ˚C glycerol stocks were streaked on solidified YPD media and cultured at 30 ˚C for 24 h. The same number of *C. neoformans* cells from each strain were suspended in sterile water, counted using a hemocytometer, and diluted to a final cell concentration of 2 × 10^6 cells/mL. In total, 3 µL serial dilutions of these cells (10^{-1} to 10^{-5}) were dropped onto YNB or L-Dopa agar media for phenotypical assay. In parallel, approximately 100 cells of H99 and *lac1*Δ were spread evenly onto YNB and L-Dopa plates and incubated in the dark at 25 ˚C. Images were

acquired on day 4 and day 10 (Figure 4.2(b)). On day 10, cells were fixed in 3.7% formaldehyde. To produce melanin ghosts, cells were incubated in 6N HCl for 2 h at 80 ˚C as described in detail previously [25].

4.2.2. Spectroscopic Collection

Spectroscopic data for *A. nidulans* strains were taken from a previous work [33,38]. In that work, progeny from a cross between FGSC A773 (wA3) and FGSC A849 (*yA2*; *rodA*Δ) [39] were collected in order to select strains that were both WT and *rodA*Δ for the hydrophobin and produced conidia of each of the three possible colors: wild type green, and mutants yellow and white, as previously described [40]. In the present study, only the data for the $rodA^{+}$ strains were used. To collect spores, each strain was grown on a separate MM plate for seven days at 30 ˚C and then harvested with 1 mL sterile distilled water using a bent glass rod, for a final concentration of 1×10^{6} spores. Spore suspensions were stored at 4 ˚C and dispersed by vortexing prior to experiments.

4.2.3. SERDS Experiments

The SERDS setup consisted of a commercial confocal Raman microscope (LabRAM HR Evolution, Horiba, Kyoto, Japan) and a homemade tunable laser emitting at ~785 nm (Figure 2.1(a), for details refer to [33, 34]). Before optical measurements, a small amount of spore suspension (6 µL) was deposited on a fused silica substrate (WG 41,010, Thorlabs, Newton, NJ, USA) and air-dried by evaporation for a few hours at 25 ˚C. The sample was then placed under the Raman microscope and excited by the tunable laser. The edge filter was used to reflect the excitation laser beam to the sample while transmitting lower-frequency (or longer-wavelength) emission signals to the spectrometer.

The pinhole blocked out-of-focus signals, thus enabling signal detection only from that part of the sample directly excited by the focused laser beam.

In order to retrieve the pure Raman spectrum of each spore according to the above SERDS technique, two spectra with slightly different laser excitation wavelengths for each spore were recorded separately. Sample numbers and laser parameters for the spectroscopic measurements of *A. fumigatus*, *A. nidulans*, and *C. neoformans* strains are listed in Tables 4.1–4.3, respectively. All raw data for *A. fumigatus* and *C. neoformans* strains are deposited and available online at [41].

Raman and fluorescence spectra corresponding to *A. nidulans* strains were taken from previously measured raw data [33,38] and processed in an identical manner as data for *A. fumigatus* and *C. neoformans* strains, according to the protocol described in the Supporting Information of [34].

Principal component analysis (PCA) was performed on the pure, retrieved Raman spectra of selected strains using the pca function in Matlab [42]. The number of spectral measurements used in PCA for strains of *A. fumigatus*, *A. nidulans*, and *C. neoformans* was equal to the sample number n in Tables 4.1–4.3.

Table 4.1. Sample and laser parameters for *A. fumigatus* strains.

A. fumigatus	***n***	$\overline{\lambda_1}$ **(nm)**	$\overline{\lambda_2}$ **(nm)**	$\overline{\Delta\nu}$ **(cm^{-1})**
WT	100	784.2	785.7	25.1
*abr2*Δ	100	784.2	785.9	26.9
*abr1*Δ	40	784.2	785.8	26.9
*arp2*Δ	40	784.2	785.8	26.9
*arp1*Δ	10	784.2	785.6	23.3
*ayg1*Δ	40	784.2	785.8	26.9
*alb1*Δ	100	784.2	785.6	23.3

Table 4.2. Sample and laser parameters for *A. nidulans* strains [33,78].

A. nidulans	***n***	$\overline{\lambda_1}$ **(nm)**	$\overline{\lambda_2}$ **(nm)**	$\overline{\Delta\nu}$ **(cm^{-1})**
WT	100	784.3	785.8	25.2
yA2	100	784.3	785.4	18.0
wA3	100	784.3	785.4	18.0

Table 4.3. Sample and laser parameters for *C. neoformans* strains.

C. neoformans	***n***	$\overline{\lambda_1}$ **(nm)**	$\overline{\lambda_2}$ **(nm)**	$\overline{\Delta\nu}$ **(cm^{-1})**
H99	40	784.1	786.0	30.5
H99 ghost	10	784.2	785.7	25.1
*lac1*Δ	100	784.1	785.7	27.1

4.3. Results and Discussion

The normalized, average background-subtracted raw spectra and the corresponding normalized average retrieved pure Raman spectra of *A. fumigatus*, *A. nidulans*, and *C. neoformans* strains are shown in Figures 4.3–4.5, respectively. In Figure 6b, the observation that the Cryptococcus H99 melanin ghost exhibits an almost identical spectrum to that of an intact cell shows that the Raman spectra indeed correspond to melanin and that the polysaccharide capsule surrounding Cryptococcus yeast cells does not significantly contribute to the measured spectrum, because the polysaccharide capsule was completely removed in the H99 ghost sample. Additionally, see, for example, the microscopic and electron spin resonance (ESR) characterizations of *C. neoformans* melanin ghosts in [43], which show that they are composed primarily of melanin. The preferential Raman excitation of melanin results from resonance with the ~785nm laser light. This is confirmed in Figure 4.6, which shows the principal component scores of the H99 (red), H99 ghost (blue) and *lac1*Δ (green) strains when jointly subjected to PCA. The H99 and H99 ghost strains are overlapping, while the *lac1*Δ strain, which does not contain

melanin but does have a polysaccharide capsule, is clearly distinct from the other two strains. These results confirm that melanin is the dominant contributor to the Raman spectrum of wild-type H99.

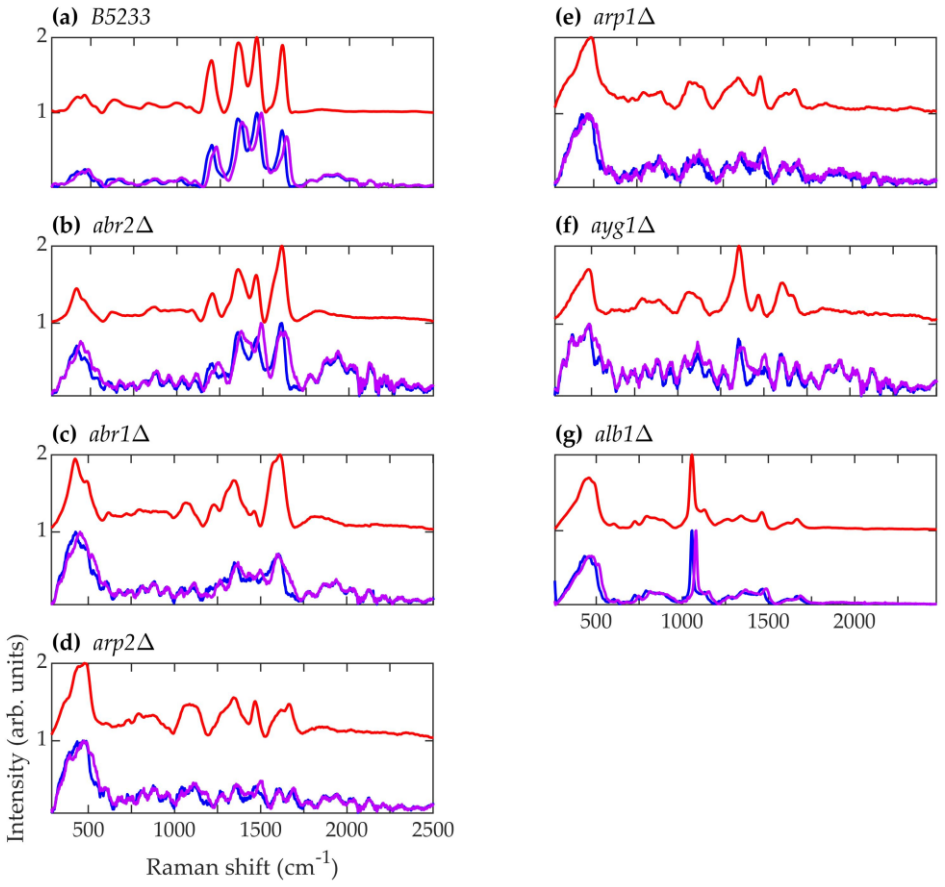

Figure 4.3. Spectra corresponding to *A. fumigatus* strains (a) B5233, (b) *abr2*Δ, (c) *abr1*Δ, (d) *arp2*Δ, (e) *arp1*Δ, (f) *ayg1*Δ, and (g) *alb1*Δ. Blue (~784.2 nm laser excitation) and purple (~785.8 nm laser excitation) curves are the average normalized background-subtracted raw spectra, while the red curves are average retrieved pure Raman spectra.

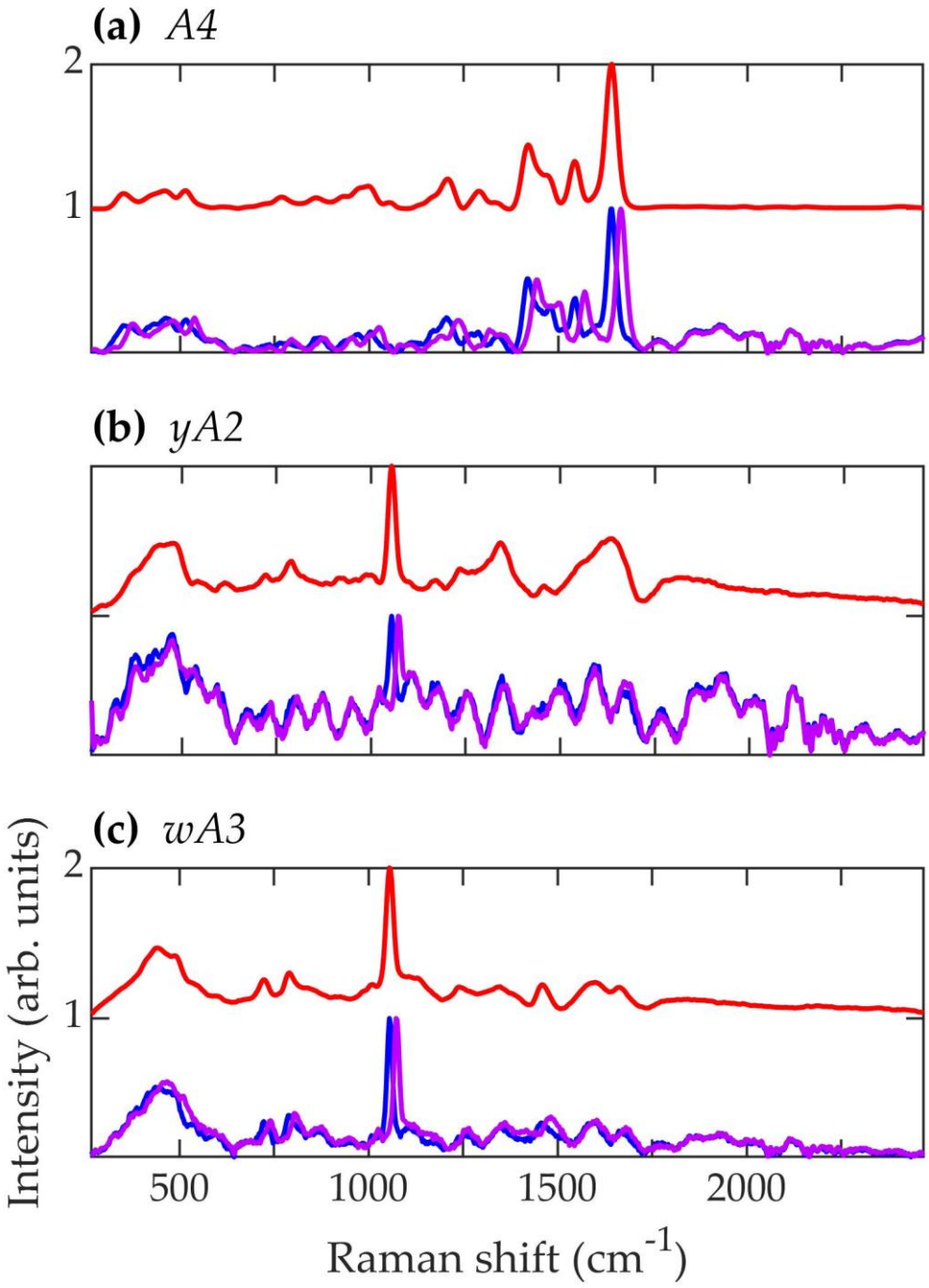

Figure 4.4. Spectra corresponding to *A. nidulans* strains (a) A4, (b) *yA*2, and (c) *wA*3. Blue (~784.3 nm laser excitation) and purple (~785.5 nm laser excitation) curves are the average normalized background-subtracted raw spectra, while the red curves are average retrieved pure Raman spectra.

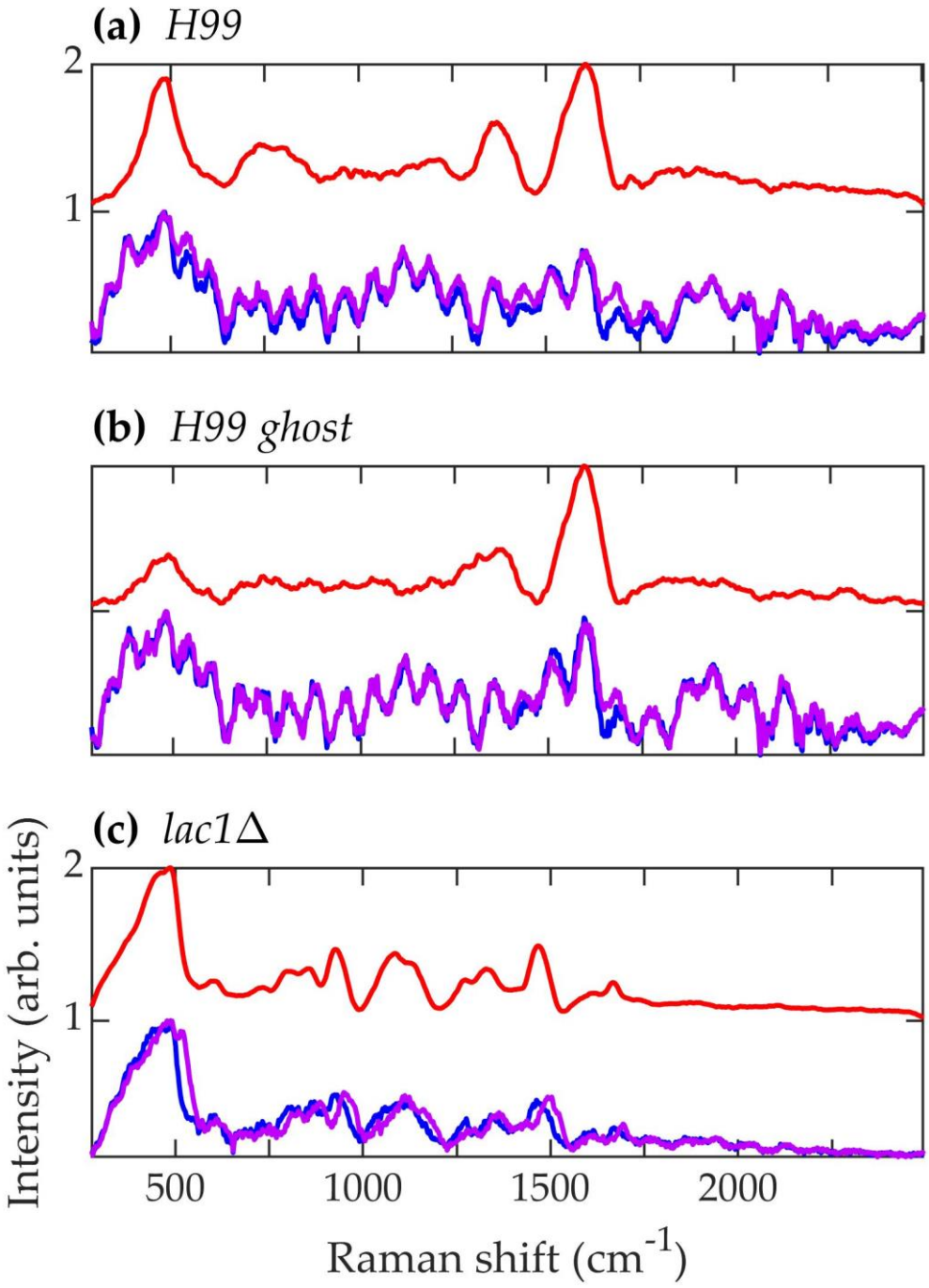

Figure 4.5. Spectra corresponding to *C. neoformans* strains (a) H99, (b) H99 ghost, and (c) *lac1*Δ. Blue (~784.1 nm laser excitation) and purple (~785.8 nm laser excitation) curves are the average normalized background-subtracted raw spectra, while the red curves are average retrieved pure Raman spectra.

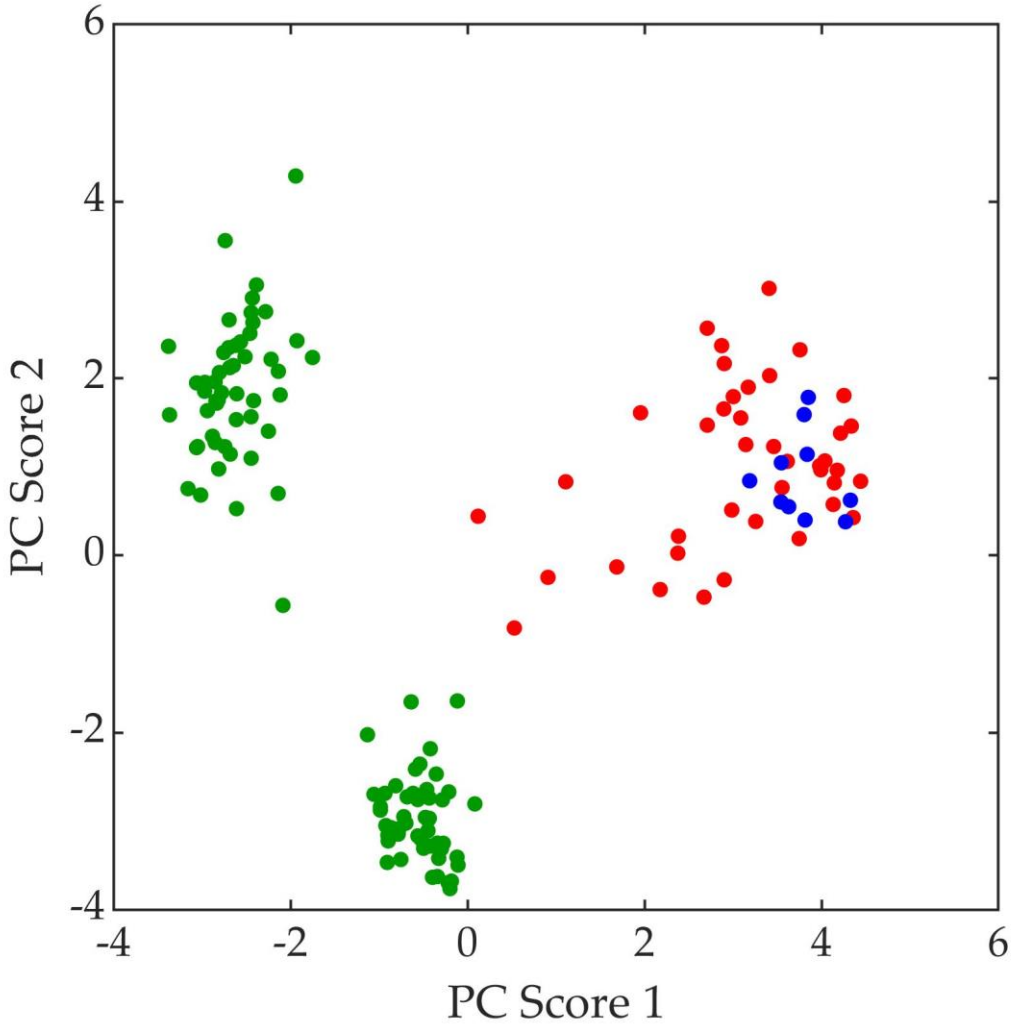

Figure 4.6. Principal component (PC) scores of *C. neoformans* strains: H99 (red), H99 ghost (blue), and *lac1*Δ (green).

Shown in Figure 4.7(a) are the average normalized retrieved pure Raman spectra of *A. fumigatus* (blue), *A. nidulans* (green), and *C. neoformans* (red) strains. The gray region surrounding each curve is the standard deviation uncertainty. Figure 4.7(b, c) shows the principal component scores of *A. fumigatus* (blue), *A. nidulans* (green), and *C.*

neoformans (red) strains at the beginning and end of each respective biosynthetic pathway. The datapoints in Figure 4.7(b, c) reflect two independent PC analyses using the pure, retrieved Raman spectral data of the strains included in each respective figure. In Figure 4.7(b), there is no clear separation of the three species if the first step of melanin biosynthesis is disrupted. In Figure 4.7(c), there is clear separation of the three species once they are melanized. This indicates that melanin is a major contributing factor in the classification.

The primary result of interest is the striking resemblance in the pure Raman spectra of the *A. nidulans* mutant strains *wA3* and *yA2* to the *alb1*Δ strain of *A. fumigatus*, namely the prominent peak at approximately 1056 cm^{-1} in Figures 4.3, 4.4 and 4.7(a). In biological tissues, this peak has been associated with lipids [44]. In the case of *A. fumigatus*, the absence in *alb1*Δ of a polyketide synthase that participates in the β-ketoacyl condensation of malonylCoA/acetyl-CoA most likely leads to a buildup of fatty acids. Since the regulatory action of malonyl-CoA inhibits the oxidation of fatty acids for metabolism [10], this leads to an increase in conversion of fatty acids to triglyceride lipids [45]. In short, a buildup of malonyl-CoA leads to a buildup of lipids. The same is likely to be true of *A. nidulans* strains, since in this species melanin biosynthesis also begins with malonyl-CoA [32]. The first enzymatic product of melanin biosynthesis in both *A. fumigatus* and *A. nidulans* is naphthopyrone [29,30]. It is therefore not surprising that mutant strains corresponding to early steps in the melanin biosynthesis process exhibit similar features in both species.

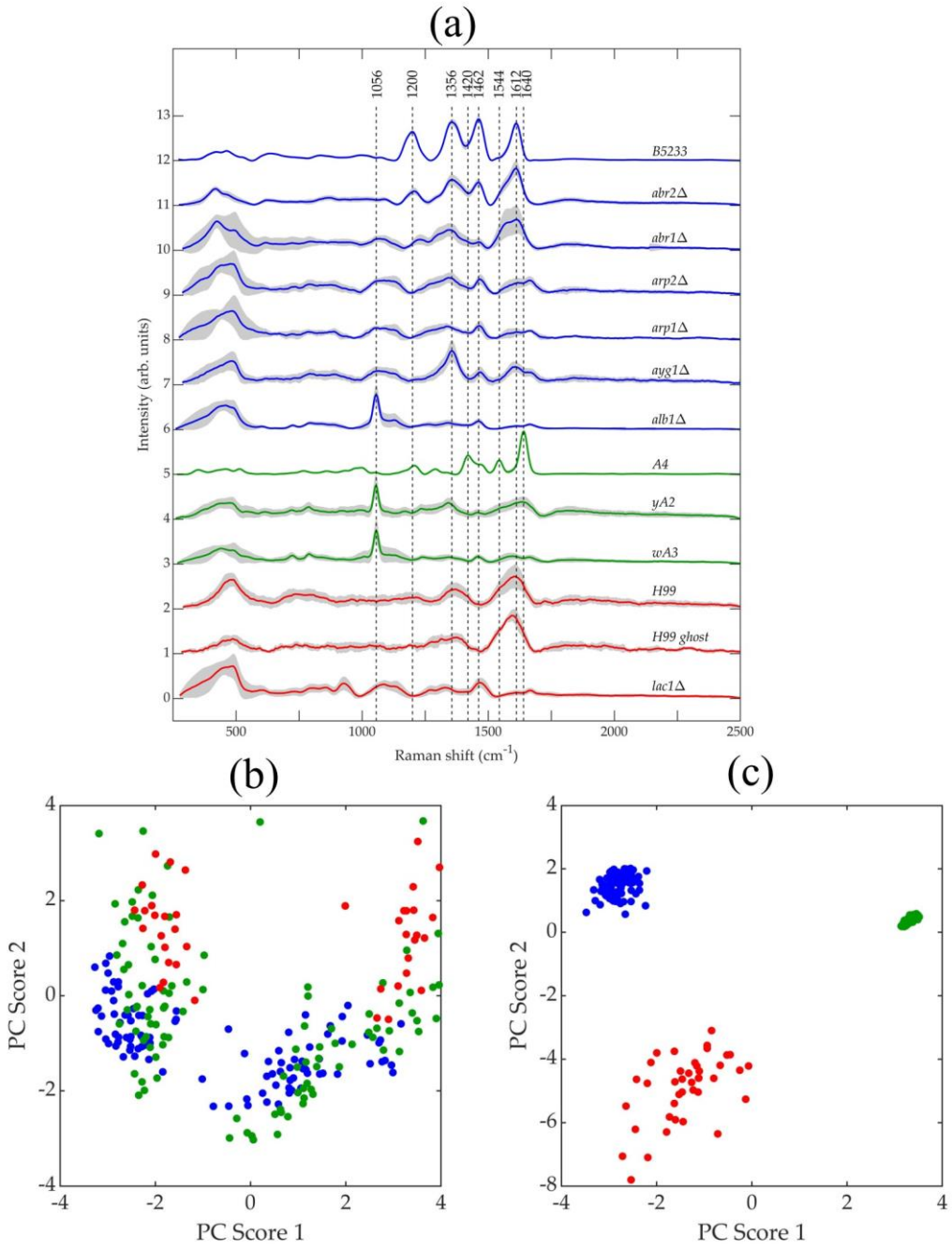

Figure 4.7. (a) Average normalized retrieved pure Raman spectra of *A. fumigatus* (blue), *A. nidulans* (green), and *C. neoformans* (red) strains. (b) Principal component scores of mutant strains at the beginning of each biosynthetic pathway: *alb1*Δ (blue), *wA3* (green), and *lac1*Δ (red). (c) Principal component scores of strains at the end of each biosynthetic pathway: B5233 (blue), A4 (green), and H99 (red).

However, the spectral features of the *A. fumigatus* and *A. nidulans* strains diverge as the melanin biosynthesis process continues in each species. This is illustrated in Figure 4.7(b, c). In Figure 4.7(b), PCA of the spectral data of each strain corresponding to the beginning of each respective biosynthetic pathway shows that *A. nidulans wA3* and *A. fumigatus alb1*Δ are largely overlapped, while *C. neoformans lac1*Δ overlaps less. In Figure 4.7(c), PCA of the spectral data of each strain corresponding to the end of each respective biosynthetic pathway shows distinct, non-overlapping groups for *A. nidulans* A4, *A. fumigatus* B5233, and *C. neoformans* H99. Indeed, the only *A. fumigatus* strain to exhibit any similarity with the *A. nidulans wA3* and *yA2* strains is *alb1*Δ, which is blocked in the very first step in the melanin metabolic pathway. The other five *A. fumigatus* mutant strains do not exhibit spectral similarity to *A. nidulans*, and in fact the fully synthesized melanin in each species likewise exhibit little similarity. We have shown in a previous work that the species *Penicillium chrysogenum* (*P. chrysogenum*) exhibits a melanin Raman spectrum (and hence melanin molecular composition and structure) of much greater similarity to *A. fumigatus* than *A. nidulans* [34]. In fact, comparison of the genes involved in melanin biosynthesis bears this out. As can be seen in Table 4.4, *P. chrysogenum* has the greatest genetic similarity to *A. fumigatus* [46]. Interestingly, a recent evolutionary study of melanin-related gene clusters suggested horizontal gene transfer between the *Aspergillus* and *Penicillium* genera [47].

Table 4.4. Melanin-related genes in *A. fumigatus* [10], *C. neoformans* [19], *A. nidulans* [32], and *P. chrysogenum* [46].

Species	*Known Melanin-Related Genes*
A. fumigatus	*pksP/alb1, ayg1, arp1, arp2, arb1, arb2*
C. neoformans	*LAC1 (major role), LAC2 (minor role)*
A. nidulans	*wA, yA*
P. chrysogenum	*pks17, ayg1, arp1, arp2, arb1, arb2*

Even though *A. fumigatus* and *A. nidulans* share the common melanin precursor naphthopyrone, it is questionable how useful it may be to classify the *A. nidulans* melanin as DHN. 1,8-dihydroxynaphthalene (DHN) is the sixth and final intermediate in the chain of biochemical reactions that leads in *A. fumigatus* from malonyl-CoA/acetyl-CoA precursors to fully polymerized melanin [1,10]. As seen in Figure 7(a, c), the *A. nidulans* Raman spectra exhibit very little similarity to the *A. fumigatus* mutant strains corresponding to advanced stages of the melanin biosynthesis pathway, and *A. nidulans* is not known to form DHN. Indeed, the prominent peaks at ~1640 and ~1544 cm^{-1} in the A4 *A. nidulans* strain have previously been identified as belonging to Amides I and II [44,48], respectively. The amide compound contains nitrogen as a key component. Melanin is classified into five categories: eumelanin, pheomelanin, neuromelanin, allomelanin, and pyomelanin. Of these, only allomelanin and pyomelanin do not contain nitrogen [49,50]. DHN melanin is classified as a major subtype of allomelanin [49]. Unlike DOPA melanin, which is classified as a eumelanin [49], DHN melanin does not contain nitrogen, and this fact is used to classify fungal melanin on the basis of nitrogen content [28]. Therefore, if the prominent ~1640 and ~1544 cm^{-1} peaks in the Raman spectrum of the A4 *A. nidulans* strain do indeed arise from Amides I and II, then the *A. nidulans* conidial melanin can be

classified neither as DHN nor as an allomelanin, even though it shares a common naphthopyrone precursor with *A. fumigatus*.

Consistent with the idea that *A. nidulans* conidial melanin should not be classified as DOPA melanin, the Raman spectra of the *A. nidulans* strains exhibit even less similarity to the *C. neoformans* strains than they do to the *A. fumigatus* strains (Figure 4.7(a–c)). The broad peaks in the *C. neoformans* H99 strain at ~1370 and ~1610 cm^{-1} mirror those observed in the Raman spectrum of DOPA melanin extracted from the sepia cuttlefish [51].

Figure 4.8 contains the average normalized background-subtracted raw spectra of *A. fumigatus* (blue), *A. nidulans* (green), and *C. neoformans* (red) strains in the range 1750–2500 cm^{-1}, which according to Figures 4.3–4.5 are composed primarily of the fluorescence signal. The gray region surrounding each curve is the standard deviation uncertainty.

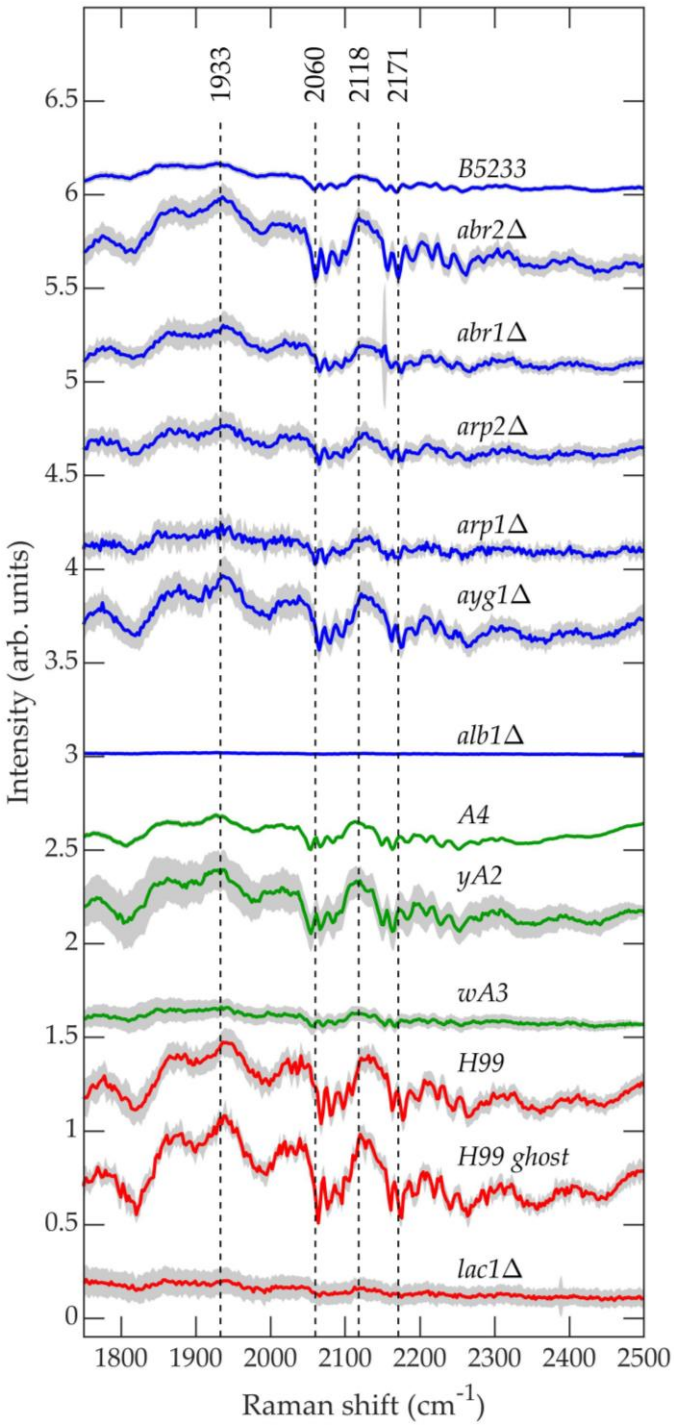

Figure 4.8. Average normalized background-subtracted raw spectra of *A. fumigatus* (blue), *A. nidulans* (green), and *C. neoformans* (red) strains in the range 1750–2500 cm^{-1}.

The fluorescence spectra shown in Figure 4.8 exhibit remarkable qualitative similarity between species, excluding the first biosynthesis pathway mutant for each, namely *A. fumigatus alb1*Δ, *A. nidulans wA3*, and *C. neoformans lac1*Δ. These three strains exhibit little or no "fine-scale fluorescence" that characterizes the spectra of the remaining strains. In a previous work, we hypothesized that the fine-scale fluorescence results from the formation of long-lived molecular cages [52,53] in the polymer matrix that constitute the cell wall, which protects the fluorescing molecules from greater levels of inhomogeneous broadening that they would otherwise experience in a liquid environment [54,55]. Figure 4.8 would suggest that the fine-scale fluorescence results from molecules associated with the onset of melanin biosynthesis. It is unknown what these molecules could be. Regardless, the fluorescence signal contains comparatively little information about molecular structure, and we have shown previously that it contains only a tiny fraction of the total information contained in the raw measured spectrum, which is dominated by the Raman contribution [34]. Nevertheless, the fine-scale fluorescence remains a feature of interest not only because its origin is unknown, but also because the mechanism that enables it might provide insight into quantum coherences in biological systems, such magnetoreception in birds, insects, and plants [56,57], for which coherence times are an active area of research [58,59].

4.4. Conclusions

We used a multi-disciplinary method to characterize the Raman spectra of melanin biosynthetic mutant strains of *A. fumigatus*, *C. neoformans*, and *A. nidulans* and used these spectra to elucidate the nature of the biosynthetic pathway of conidial melanin in *A.*

nidulans. We find that the dissimilarity between the *C. neoformans* and conidial *A. nidulans* Raman spectra excludes the possibility that the *A. nidulans* conidial pigment may be associated with the DOPA biosynthesis pathway. We also find that the *A. nidulans* conidial melanin cannot straightforwardly be classified as belonging to the DHN pathway. While the spectral similarity of the *A. nidulans wA3* and *yA2* strains to the *A. fumigatus alb1*Δ strain confirms that they share common melanin precursors, namely malonyl-CoA/acetylCoA and naphthopyrone, the spectral divergence exhibited by mutant and wild-type strains further along their respective melanin biosynthetic pathways suggests that the fully polymerized melanin differ in structure and perhaps in composition. Moreover, the main ~1640 and ~1544 cm^{-1} peaks in the wild-type A4 strain of *A. nidulans* have been identified as belonging to Amides I and II [44,48], and, if this is indeed the case, the *A. nidulans* conidial melanin cannot be classified as DHN.

We anticipate that the multi-disciplinary approach detailed above will find increasing use in the characterization of fungal melanin, which have great potential for powerful and eco-friendly breakthroughs in industry and medicine.

4.5. References

[1] Pombeiro-Sponchiado, S.R.; Sousa, G.S.; Andrade, J.C.R.; Lisboa, H.F.; Gonçalves, R.C.R. Production of melanin pigment by fungi and its biotechnological applications. In Melanin; IntechOpen: London, UK, 2017.

[2] Pralea, I.-E.; Moldovan, R.-C.; Petrache, A.-M.; Ilies, , M.; Heghes, , S.-C.; Ielciu, I.; Nicoară, R.; Moldovan, M.; Ene, M.; Radu, M.; et al. From extraction to advanced analytical methods: The challenges of melanin analysis. Int. J. Mol. Sci. 2019, 20, 3943.

[3] Chang, P.-K.; Cary, J.W.; Lebar, M.D. Biosynthesis of conidial and sclerotial pigments in Aspergillus species. Appl. Microbiol. Biotechnol. 2020, 104, 2277–2286.

[4] Latgé, J.-P. Aspergillus fumigatus and Aspergillosis. Clin. Microbiol. Rev. 1999, 12, 310–350.

[5] Wilson, B.J. Miscellaneous Aspergillus toxins. In Microbial Toxins; Holst, O., Ed.; Academic Press: Cambridge, UK, 1971; Volume 6, pp. 207–295. ISBN 978-1-4939-8351-3.

[6] Fungal Infections, Aspergillus fumigatus. Available online: http://www.life-worldwide.org/fungal-diseases/aspergillusfumigatus (accessed on 23 July 2020).

[7] Nosanchuk, J.D.; Stark, R.E.; Casadevall, A. Fungal melanin: What do we know about structure? Front. Microbiol. 2015, 6, 1463.

[8] Latge, J.-P. The Fungal Cell Wall: An Armour and a Weapon for Human Fungal Pathogens; Latge, J.-P., Ed.; Current Topics in Microbiology and Immunology; Springer: Berlin/Heidelberg, Germany, 2020; Volume 425, ISBN 978-3-030-49927-0.

[9] Tsai, H.-F.; Wheeler, M.H.; Chang, Y.C.; Kwon-Chung, K.J. A developmentally regulated gene cluster involved in conidial pigment biosynthesis in Aspergillus fumigatus. J. Bacteriol. 1999, 181, 6469–6477.

[10] Perez-Cuesta, U.; Aparicio-Fernandez, L.; Guruceaga, X.; Martin-Souto, L.; DE Cerio, A.A.D.; Antoran, A.; Buldain, I.; Hernando, F.L.; Martin-Souto, L.; Rementeria, A. Melanin and pyomelanin in Aspergillus fumigatus: From its genetics to host interaction. Int. Microbiol. 2019, 23, 55–63.

[11] Upadhyay, S.; Torres, G.; Lin, X. Laccases involved in 1,8-dihydroxynaphthalene melanin biosynthesis in Aspergillus fumigatus are regulated by developmental factors and copper homeostasis. Eukaryot. Cell 2013, 12, 1641–1652. [CrossRef] [PubMed]

[12] Upadhyay, S.; Xu, X.; Lin, X. Interactions between melanin enzymes and their atypical recruitment to the secretory pathway by palmitoylation. mBio 2016, 7, e01925-16.

[13] Upadhyay, S.; Xu, X.; Lowry, D.; Jackson, J.C.; Roberson, R.W.; Lin, X. Subcellular compartmentalization and trafficking of the biosynthetic machinery for fungal melanin. Cell Rep. 2016, 14, 2511–2518.

[14] Chun, C.D.; Madhani, H.D. Applying genetics and molecular biology to the study of the human pathogen Cryptococcus neoformans. In Methods in Enzymology; Weissman, J., Guthrie, C., Fink, G.R., Eds.; Guide to Yeast Genetics: Functional Genomics, Proteomics, and other Systems Analysis; Academic Press: Cambridge, UK, 2010; Volume 470, pp. 797–831.

[15] Buchanan, K.L. What makes Cryptococcus neoformans a pathogen? Emerg. Infect. Dis. 1998, 4, 71–83.

[16] Casadevall, A.; Rosas, A.L.; Nosanchuk, J.D. Melanin and virulence in Cryptococcus neoformans. Curr. Opin. Microbiol. 2000, 3, 354–358.

[17] McFadden, D.C.; Casadevall, A. Capsule and melanin synthesis in Cryptococcus Neoformans. Med. Mycol. 2001, 39, 19–30.

[18] Perfect, J.R. Cryptococcus neoformans: A sugar-coated killer with designer genes. FEMS Immunol. Med. Microbiol. 2005, 45, 395–404.

[19] Pukkila-Worley, R.; Gerrald, Q.D.; Kraus, P.R.; Boily, M.-J.; Davis, M.J.; Giles, S.S.; Cox, G.M.; Heitman, J.; Alspaugh, J.A. Transcriptional network of multiple capsule and melanin genes governed by the Cryptococcus neoformans cyclic AMP cascade. Eukaryot. Cell 2005, 4, 190–201.

[20] Prota, G. Melanins and Melanogenesis; Academic Press: Cambridge, UK, 1992; ISBN 978-0-12-565970-3.

[21] Polacheck, I.; Kwon-Chung, K.J. Melanogenesis in Cryptococcus neoformans. J. Gen. Microbiol. 1988, 134, 1037–1041.

[22] Williamson, P.R.; Wakamatsu, K.; Ito, S. Melanin biosynthesis in Cryptococcus neoformans. J. Bacteriol. 1998, 180, 1570–1572.

[23] Hicks, J.K.; D'Souza, C.A.; Cox, G.M.; Heitman, J. Cyclic AMP-dependent protein kinase catalytic subunits have divergent roles in virulence factor production in two varieties of the fungal pathogen Cryptococcus neoformans. Eukaryot. Cell 2004, 3, 14–26.

[24] Lee, D.; Jang, E.-H.; Lee, M.; Kim, S.-W.; Lee, Y.; Lee, K.-T.; Bahn, Y.-S. Unraveling melanin biosynthesis and signaling networks in Cryptococcus neoformans. mBio 2019, 10, e02267-19.

[25] Camacho, E.; Vij, R.; Chrissian, C.; Prados-Rosales, R.; Gil, D.; O'Meally, R.N.; Cordero, R.J.B.; Cole, R.N.; McCaffery, J.M.; Stark, R.E.; et al. The structural unit of melanin in the cell wall of the fungal pathogen Cryptococcus neoformans. J. Biol. Chem. 2019, 294, 10471–10489.

[26] Pirt, S.J.; Rowley, B.I. Melanin production in Aspergillus nidulans. Biochem. J. 1969, 114, 9P–10P.

[27] Bull, A.T. Chemical composition of wild-type and mutant Aspergillus nidulans cell walls. The nature of polysaccharide and melanin constituents. J. Gen. Microbiol. 1970, 63, 75–94.

[28] Gonçalves, R.C.R.; Lisboa, H.C.F.; Pombeiro-Sponchiado, S.R. Characterization of melanin pigment produced by Aspergillus nidulans. World J. Microbiol. Biotechnol. 2012, 28, 1467–1474.

[29] Watanabe, A.; Fujii, I.; Sankawa, U.; Mayorga, M.E.; Timberlake, W.E.; Ebizuka, Y. Re-identification of Aspergillus nidulans wA gene to code for a polyketide synthase of naphthopyrone. Tetrahedron Lett. 1999, 40, 91–94.

[30] Tsai, H.-F.; Fujii, I.; Watanabe, A.; Wheeler, M.H.; Chang, Y.C.; Yasuoka, Y.; Ebizuka, Y.; Kwon-Chung, K.J. Pentaketide melanin biosynthesis in Aspergillus fumigatus requires chain-length shortening of a heptaketide precursor. J. Biol. Chem. 2001, 276, 29292–29298.

[31] Wheeler, M.H.; Bell, A.A. Melanins and their importance in pathogenic fungi. In Current Topics in Medical Mycology; Springer: Berlin/Heidelberg, Germany, 1988; pp. 338–387.

[32] Klejnstrup, M.L.; Frandsen, R.J.N.; Holm, D.K.; Nielsen, M.T.; Mortensen, U.H.; Larsen, T.O.; Nielsen, J.B. Genetics of polyketide metabolism in Aspergillus nidulans. Metabolites 2012, 2, 100–133.

[33] Han, Z.; Strycker, B.D.; Commer, B.; Wang, K.; Shaw, B.D.; Scully, M.O.; Sokolov, A.V. Molecular origin of the Raman signal from Aspergillus nidulans conidia and observation of fluorescence vibrational structure at room temperature. Sci. Rep. 2020, 10, 5428.

[34] Strycker, B.D.; Han, Z.; Duan, Z.; Commer, B.; Wang, K.; Shaw, B.D.; Sokolov, A.V.; Scully, M.O. Identification of toxic mold species through Raman spectroscopy of fungal conidia. PLoS ONE 2020, 15, e0242361.

[35] Butler, H.; Ashton, L.; Bird, B.; Cinque, G.; Curtis, K.; Dorney, J.; Esmonde-White, K.; Fullwood, N.J.; Gardner, B.; MartinHirsch, P.L.; et al. Using Raman spectroscopy to characterize biological materials. Nat. Protoc. 2016, 11, 664–687.

[36] Pacelli, C.; Cassaro, A.; Maturilli, A.; Timperio, A.M.; Gevi, F.; Cavalazzi, B.; Stefan, M.; Ghica, D.; Onofri, S. Multidisciplinary characterization of melanin pigments from the black fungus Cryomyces antarcticus. Appl. Microbiol. Biotechnol. 2020, 104, 6385–6395.

[37] Mattoon, E.; Cordero, R.; Casadevall, A. Fungal melanins and applications in healthcare, bioremediation and industry. J. Fungi 2021, 7, 488.

[38] Han, Z. Molecular origin of the Raman signal from Aspergillus nidulans conidia and observation of fluorescence vibrational structure at room temperature. OSF 2020, 10, 1–8.

[39] McCluskey, K.; Wiest, A.; Plamann, M. The fungal genetics stock center: A repository for 50 years of fungal genetics research. J. Biosci. 2010, 35, 119–126.

[40] Kaminskyj, S.G.W. Fundamentals of growth, storage, genetics and microscopy of Aspergillus nidulans. Fungal Genet. Rep. 2001, 48, 25–31.

[41] Han, Z. Raman characterization of fungal DHN and DOPA melanin biosynthesis pathways. OSF 2021.

[42] Pca; The MathWorks, Inc. 2012. Available online: https://www.mathworks.com/help/stats/pca.html (accessed on 1 October 2021).

[43] Wang, Y.; Aisen, P.; Casadevall, A. Melanin, melanin "ghosts" and melanin composition in Cryptococcus neoformans. Infect. Immun. 1996, 64, 2420–2424.

[44] Movasaghi, Z.; Rehman, S.; Rehman, I.U. Raman spectroscopy of biological tissues. Appl. Spectrosc. Rev. 2007, 42, 493–541.

[45] Clarke, S.D.; Nakamura, M.T. Fatty acid synthesis and its regulation. Encycl. Biol. Chem. 2004, 1, 99–103.

[46] Samol, M.M. Genomic Wake-up Call: Activating Silent Biosynthetic Pathways for Novel Metabolites in Penicillium Chrysogenum; University of Groningen: Groningen, The Netherlands, 2015.

[47] Jia, S.-L.; Chi, Z.; Chen, L.; Liu, G.-L.; Hu, Z.; Chi, Z.-M. Molecular evolution and regulation of DHN melanin-related gene clusters are closely related to adaptation of different melanin-producing fungi. Genomics 2021, 113, 1962–1975.

[48] Farazkhorasani, F. Raman and SERS Studies of Filamentous Fungi. Master's Thesis, University of Manitoba, Winnipeg, MB, Canada, 2014.

[49] Cao, W.; Zhou, X.; McCallum, N.C.; Hu, Z.; Ni, Q.Z.; Kapoor, U.; Heil, C.M.; Cay, K.S.; Zand, T.; Mantanona, A.J.; et al. Unraveling the structure and function of melanin through synthesis. J. Am. Chem. Soc. 2021, 143, 2622–2637.

[50] McCallum, N.C.; Son, F.A.; Clemons, T.D.; Weigand, S.J.; Gnanasekaran, K.; Battistella, C.; Barnes, B.E.; Abeyratne-Perera, H.; Siwicka, Z.E.; Forman, C.J.; et al. Allomelanin: A biopolymer of intrinsic microporosity. J. Am. Chem. Soc. 2021, 143, 4005–4016.

[51] Centeno, S.A.; Shamir, J. Surface enhanced Raman scattering (SERS) and FTIR characterization of the sepia melanin pigment used in works of art. J. Mol. Struct. 2008, 873, 149–159.

[52] Cicogna, F.; Coiai, S.; Pinzino, C.; Ciardelli, F.; Passaglia, E. Fluorescent polyolefins by free radical post-reactor modification with functional nitroxides. React. Funct. Polym. 2012, 72, 695–702.

[53] Prampolini, G.; Monti, S.; De Mitri, N.; Barone, V. Evidences of long lived cages in functionalized polymers: Effects on chromophore dynamic and spectroscopic properties. Chem. Phys. Lett. 2014, 601, 134–138.

[54] Valeur, B.; Berberan-Santos, M.N. Molecular Fluorescence: Principles and Applications; John and Wiley Sons: Hoboken, NJ, USA, 2002; ISBN 978-3-527-32846-8.

[55] Turro, N.J.; Ramamurthy, V.; Scaiano, J.C. Modern molecular photochemistry of organic molecules. Photochem. Photobiol. 2012, 88, 1033.

[56] Lloyd, S. Quantum coherence in biological systems. J. Phys. Conf. Ser. 2011, 302, 012037.

[57] Galland, P.; Pazur, A. Magnetoreception in plants. J. Plant Res. 2005, 118, 371–389.

[58] Gauger, E.M.; Rieper, E.; Morton, J.J.L.; Benjamin, S.C.; Vedral, V. Sustained quantum coherence and entanglement in the avian compass. Phys. Rev. Lett. 2011, 106, 040503.

[59] Jain, R.; Poonia, V.S.; Saha, K.; Saha, D.; Ganguly, S. The avian compass can be sensitive even without sustained electron spin coherence. Proc. R. Soc. A Math. Phys. Eng. Sci. 2021, 477, 20200778.

5. CARS SPECTROSCOPY OF ASPERGILLUS NIDULANS SPORES*

Coherent Anti-Stokes Raman Spectroscopy (CARS) is performed on single spores (conidia) of the fungus *Aspergillus nidulans* in order to establish a baseline measurement for fungal spores. Chemical maps of single spores are generated and spectral differentiation between the cell wall and the cytoplasm is achieved. Principal Component Analysis of the measured spectra is then completed as a means to quantify spore heterogeneity. Applications range from the quick and accurate diagnosis of public health concerns to real-time agricultural and environmental sensing of fungal symbionts and pathogens.

5.1. Induction

A technically powerful counterpart to spontaneous Raman spectroscopy is Coherent Anti-Stokes Raman Spectroscopy (CARS), which possesses several advantages over spontaneous Raman. The spontaneous Raman signal intensity I_S is proportional to the number of target molecules N such that $I_S \propto N$. The CARS process, however, induces a molecular coherence, resulting in a signal intensity I_{CARS} that is proportional to the square of the number of target molecules, such that $I_{CARS} \propto N^2$. Consequently, the molecular coherence of the CARS process is able to provide a comparable signal-to-noise ratio to a spontaneous Raman process using integration times that are faster by at least two orders of magnitude [1].

* Copyright © 2020 Han et al. Reprinted/adapted with permission from "Molecular origin of the Raman signal from Aspergillus nidulans conidia and observation of fluorescence vibrational structure at room temperature" by Zehua Han et al. Sci Rep 10, 5428 (2020).

There is a large body of literature documenting the use of CARS in characterizing biological tissues and cells. Sophisticated, optimized schemes such as FAST-CARS have received significant attention in the application of quick and accurate identification of bacterial endospores to combat the threat of biological terrorism, even achieving single-pulse spectral characterization [2–4]. To date, however, no coherent Raman technique has been applied to the study of mold spores. In this paper we report the first such demonstration of CARS, a two-pulse broadband scheme applied in particular to the rapid spectral analysis and characterization of spores (conidia) of the fungus *Aspergillus nidulans* (*A. nidulans*). We envision that, in the future, the technique will be applied to real-time identification of fungal spores and mycotoxins in domestic, commercial, and agricultural settings, thus addressing the pressing public health and economic needs that continue to be so costly.

5.2. Materials and Methods

5.2.1. Sample Preparation

The *A. nidulans* wild-type strain FGSC A4 [5] was grown on minimal medium, prepared as previously described [6], and incubated at 30 °C under continuous light. After 7 days, cultures were flooded with 2 mL sterile water and scraped with a sterile glass rod to release conidia (hereafter called spores). The spore suspension was washed at least three times by centrifugation (1 min. at 13,000 rpm) and stored in 1 mL sterile water at 4 °C. For experiments designed to examine cell walls of spores, 200 mg autoclaved glass beads (0.5 mm, Bio-Spec, Bartlesville, OK) were added to a subset of the sample and cells were

disrupted for 15–20 s using a tissue homogenizer (Mini-Beadbeater, BioSpec, Bartlesville, OK).

To deposit the spores upon a microscope glass slide for subsequent CARS analysis, 8.7 μL of the spore suspension was pipetted onto the glass slide and evaporated at room temperature for several hours until only the spores remained. No spores that remained upon the glass slide for more than 24 hours were analyzed; new spore samples were pipetted from the suspension for each day's experiments, so that the moisture content of the spores used was held constant.

5.2.2. CARS Experiments

The experimental layout shown in Figure 5.1 is based on that of Yujie Shen and coworkers [7]. A Nd:YVO_4 laser (Attodyne Inc, APLX-10) produced pulses 7 ps in duration at 1064 nm with a repetition rate of 1 MHz. After passing through an isolator (Thorlabs, IO-5-1064-VHP), the output pulses were divided into two arms. Two pairs of half-wave plates and polarizing beam-splitters were used to control the power in the two arms, respectively. One arm, which contained a delay stage, served as the pump/probe beam. The other beam was converged by a lens (Thorlabs, LA1509-C) into a 2-m-long photonic crystal fiber (NKT Photonics, LMA-20) to generate broadband Stokes pulses, and then subsequently collimated by an off-axis parabolic mirror (Thorlabs, MPD129-P01). The Stokes beam was then propagated through a long-pass filter (Thorlabs, FELH1150) to remove shorter wavelength components before re-combination with the pump/probe beam through a dichroic beam splitter (Semrock Inc, LPD02-1064U-25). The delay stage was varied to control the temporal overlap between the two beams, and a linear

polarizer (Thorlabs, LPNIR100-MP) was employed to maintain identical polarization. Subsequently, the two combined beams were focused by a 40X reflective objective (Thorlabs, LMM-40X-P01, 0.5 N.A.) and spatially overlapped on the sample. Both pump/probe and Stokes beams had a laser spot size approximately 2 μm in diameter, yielding a lateral spatial resolution of about 1 μm, which was also the minimum step size of the motorized stage (Prior Sci, ES111) upon which the sample was mounted.

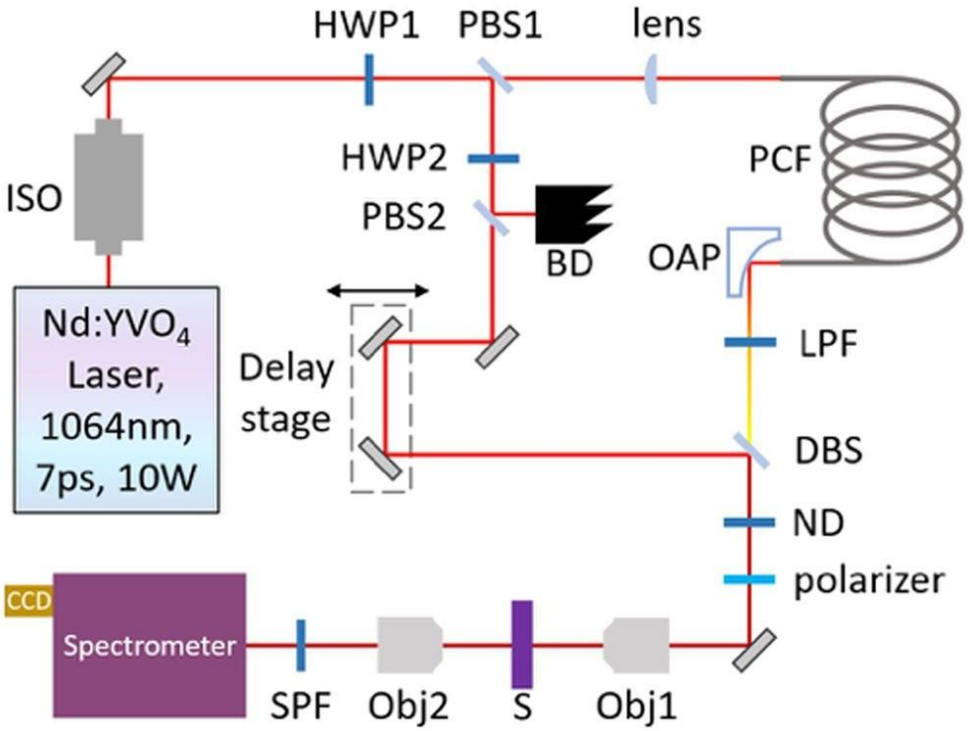

Figure 5.1. Schematic diagram of the experimental setup. ISO: isolator; HWP: half-wave plate; PBS: polarizing beam-splitter; PCF: photonic crystal fiber; OAP: off-axis parabolic mirror; LPF: long-pass filter; BD: beam dump; DBS: dichroic beam-splitter; ND: neutral density filter; Obj: microscope objective; S: sample; SPF: shortpass filter.

In addition to providing a much stronger signal compared to the spontaneous Raman setups of both Ghosal et al [8] and Farazkhorasani [9], our CARS

microspectroscopy apparatus was transmissive. The CARS signal was collected by a 20X microscope objective (YSC Technologies, Plan Fluor, 0.45 N.A.) in the forward direction, followed by a short-pass filter (Thorlabs, FESH1000) and then sent into a spectrometer (Andor Inc, Holospec) to be detected by a CCD (Andor Inc, iDus416). All CARS spectra were taken using a beam power of 1.65 mW for the pump/probe beam and 0.95 mW for the Stokes beam, as measured with a powermeter (Thorlabs, S175C). See APPENDIX A for a characterization of the measured CARS spectra using different beam powers as a function of time.

5.2.3. Data Processing

Multiple CARS spectra were taken from each intact spore (n = 99) and from lysed spores (n = 17). Because of the biological variability of the spores, the non-resonant background of each measured CARS spectrum varied considerably. To correct for this large variation and to provide a standard of comparison for the measured spectra, the non-resonant background of each spectrum was subtracted with a 9th order polynomial algorithm (*subback* function, based upon [10], of the Biodata toolbox for MATLAB [11]) and then normalized by the subsequent CARS spectrum of the glass microscope slide upon which the fungal spores were deposited. Spectral normalization by the CARS spectrum of the glass substrate corrects for the varying spectral intensity of the supercontinuum probe pulse, under the condition that the glass substrate has no Raman resonances over the wavenumber range of the measurement (which is indeed the case here) [12–14]. The corrected CARS spectra therefore contain minimal contribution from the glass microscope

slides and are primarily representative of the spores only. Finally, each resulting CARS spectrum was normalized with respect to the area under the curve.

For a subset (n = 48) of the intact spores mentioned above, the minimum diameter was able to be measured using image analysis software (ImageJ), calibrated with a resolution test target (R1DS1N, Thorlabs). In order to determine the relationship of spore diameter to measured CARS spectral variation, Principal Component Analysis (PCA) of the corrected and averaged CARS spectra of the edge and center of the spores was conducted. The average spectrum of the edge and center of each spore was calculated using the spectra corresponding to a radius of 1.2 and 0 μm, respectively. From the average spectrum (edge or center, respectively) of each of the n = 48 spores, a spectral correlation matrix was constructed using the Pearson correlation coefficient. The eigenvector corresponding to the largest eigenvalue of the matrix was then used to calculate the Principal Component (PC) score of each corrected spectrum.

Additionally, several CARS spectra of intact spores were taken using a sapphire substrate and, besides normalizing by the peak amplitude, were not processed in any way.

5.3. Results and Discussion

9 μm × 9 μm CARS maps were generated for each of 99 single, intact *A. nidulans* spores, each with a pixel resolution of 1 μm × 1 μm and an integration time of 1 s per CARS spectrum per pixel. The corrected spectra of each pixel were then averaged over the 99 spores in order to construct a single CARS map of an "average spore." The result of this procedure is graphed in Figure 5.2 (bottom), which shows the spectral similarity (calculated by the Pearson correlation coefficient) of each pixel's averaged spectrum as

referenced to the averaged spectrum of a point on the edge of the spore with coordinates (0,2). The reference spectrum on the edge of the spore is graphed in blue in Figure 5.3, while the spectrum of the conspicuous pixel with coordinates (0,0) in the middle of the spore is graphed in red in Figure 5.3. Both the red and the blue spectra in Figure 5.3 are used as reference spectra in subsequent calculations.

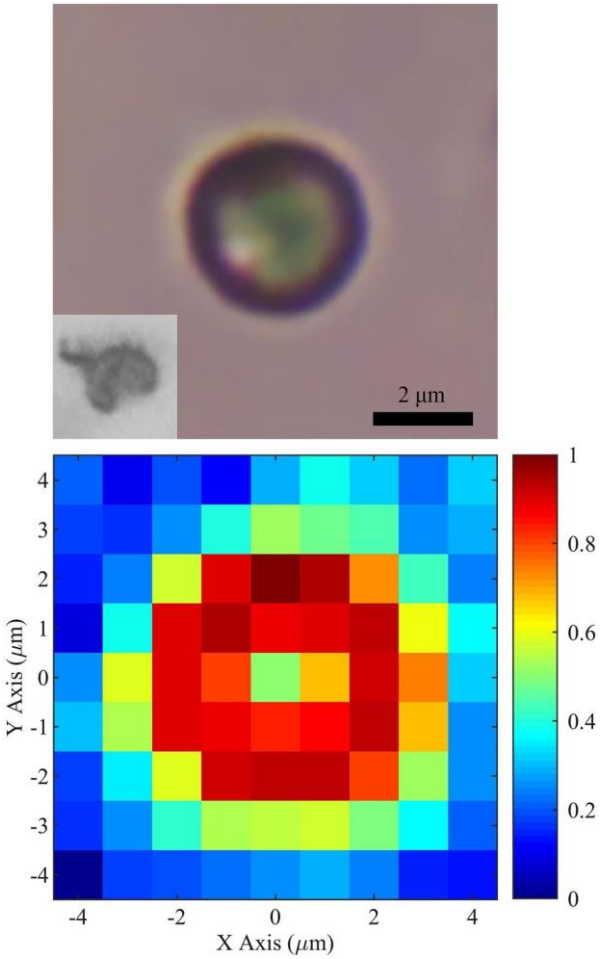

Figure 5.2. Top: optical image of an intact spore (conidium) of the fungus *A. nidulans*. The inset shows a lysed spore. Bottom: spectral similarity (calculated by the Pearson correlation coefficient) constructed from the average of 99 CARS maps of single, intact *A. nidulans* spores. The reference spectrum has coordinates (0,2) and is graphed in blue in Figure 5.3. The spectrum of the middle of the spore with coordinates (0,0) is graphed in red in Figure 5.3. Pixels surrounding the spore correspond to the glass substrate.

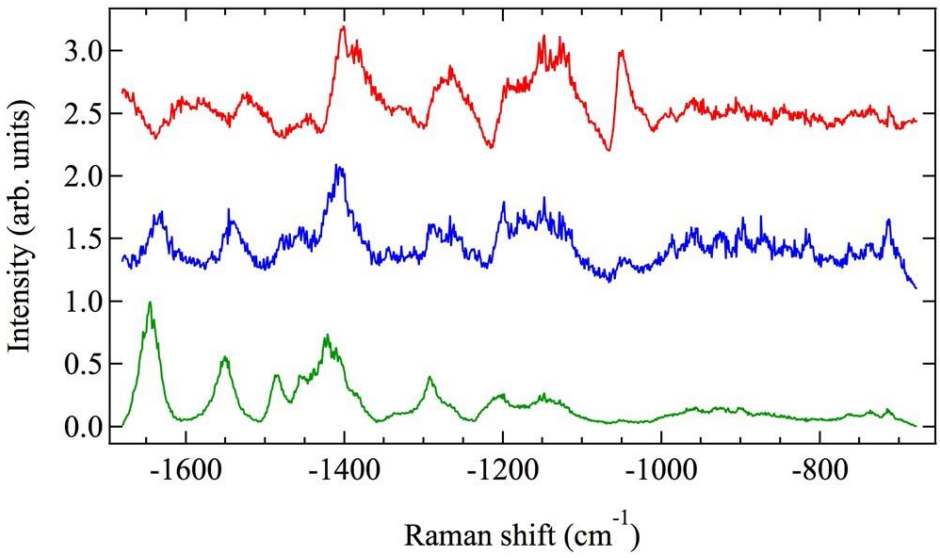

Figure 5.3. Corrected and averaged CARS spectra. Red and blue spectra belong to Fig. 2 (bottom) coordinates (0,0) and (0,2), respectively, and have been averaged over 99 intact spores. The green spectrum is the corrected and averaged CARS spectrum of 56 individual pixels from a total of 17 lysed spores and is the average CARS spectrum from the spore cell wall alone.

The relationship between the CARS spectra in the middle and edge of the spore becomes more apparent if the azimuthal symmetry of the spores is used to average the data in the radial direction, as well. The result of averaging in the radial direction is shown in Figure 5.4, where the (0,0) coordinate in Figure 5.2 (bottom) is taken as the zero radius. The red curve shows the average similarity of the CARS spectra measured at a given radius (for all 99 sampled spores) referenced to the red CARS spectrum in Figure 5.3, which corresponds to the middle of the spore. The blue curve in Figure 5.4 shows the average similarity at a given radius (again, for all 99 sampled spores) referenced to the blue spectrum in Figure 5.3, which corresponds to the edge of the spore. The error bars show the standard deviation of the mean.

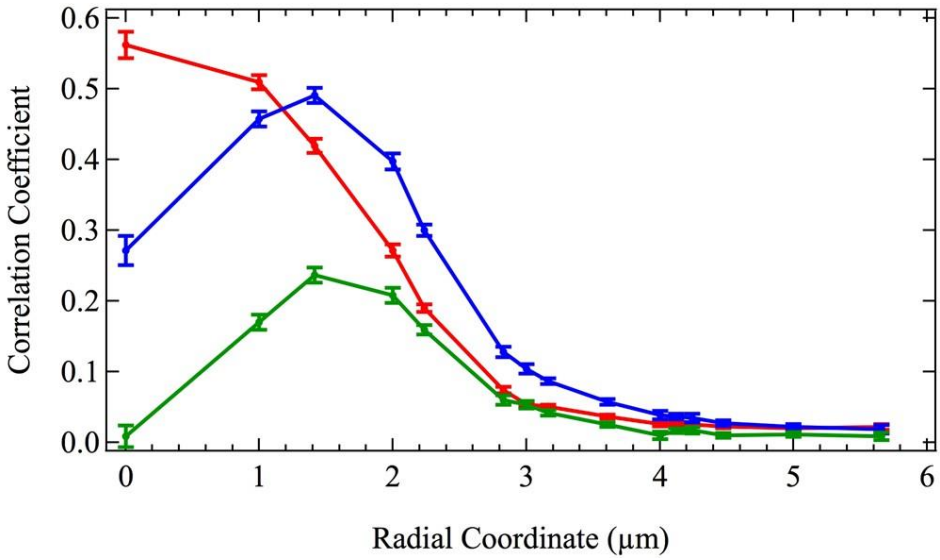

Figure 5.4. Spectral similarity of CARS spectra (calculated by the Pearson correlation coefficient) as a function of radius averaged over 99 intact spores. Red, blue, and green curves correspond to the reference CARS spectra shown in red, blue, and green in Figure 5.3, respectively, which are the middle, edge, and cell wall of *A. nidulans* spores. Error bars show the standard deviation of the mean.

The similarity curves in Figure 5.4, along with previously published transmission electron micrographs of *A. nidulans* spores [15], suggest that CARS measurements taken in the middle of the spore correspond primarily to the cytoplasm, while CARS measurements taken at the edge of the spore correspond to the cell wall. In order to test this hypothesis, a sample of the spores was lysed with glass beads in order to fracture and separate the cell wall from the cytoplasm. The CARS spectra of the cell walls of 17 lysed spores were then measured, for a total of 56 CARS spectra. The average CARS spectrum of these 56 measurements of the cell wall of lysed spores is shown in green in Figure 5.3. It is similar in shape to the spontaneous Raman spectrum of *A. nidulans* spores published by Farazkhorasani [9], although there are minor differences because of the expected contribution from the non-resonant background of the CARS process [12-14]. This

average CARS spectrum of the cell wall of the spores is used as a reference spectrum for the green similarity curve in Figure 5.4, which shows the average similarity of the measured CARS spectra of the 99 intact spores as a function of radius. It is important to note that the similarity of the 99 spores calculated in reference to a CARS spectrum consisting only of the cell wall peaks at the edge of the spore and is zero at zero radius, indicating that CARS measurements taken in the middle of intact spores correspond primarily to the cytoplasm, while those taken at the edge of the spore correspond primarily to the cell wall.

The differences in the CARS spectra for the edge and center of the intact spores arise from the differing geometry and chemical compositions of these structures. When dry and dormant, the cell wall has three layers. The outermost layer is approximately 7–14 nm thick and is composed of hydrophobin protein rodlet structures [16,17]. The inner two layers are 126–252 nm and 140–224 nm thick, respectively, and are composed primarily of glucan and chitin [16,18,19]. Separating the layered cell wall from the inner cytoplasm is the cell membrane composed of a bilayer of lipids [20]. The cytoplasm contains the organelles of the cell as well as deposits of energy-rich molecules. Molecules found in the cytoplasm include nucleotides, proteins, polysaccharides, and lipids, among many others [16,21].

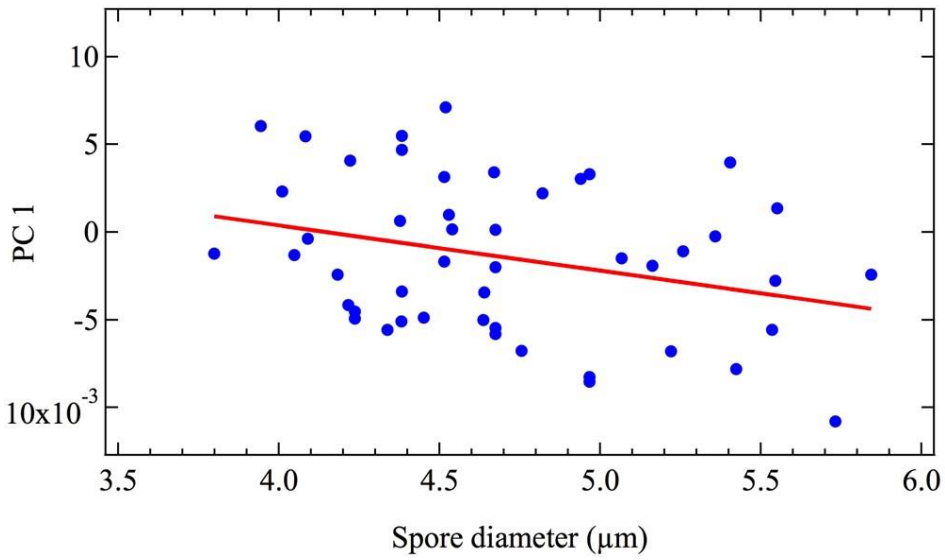

Figure 5.5. The primary PC scores of the average spectra of the edge of single spores of *A. nidulans* versus their minimum diameter. Data points are graphed in blue, while a linear fit is shown in red.

Since the cell wall has a finite thickness ranging from 273–490 nm and surrounds the entirety of the cytoplasm, CARS spectra corresponding to the edge of the spore contain Raman contributions primarily from the cell wall. CARS spectra corresponding to the middle of the spore contain Raman contributions primarily from the cytoplasm, as mentioned above and shown in Figure 5.4. The different ensembles of molecules contained in these two sampling regions of the spore result in the collection of Raman peaks shown in Figure 5.3. The spectra are indicative of the total contribution from each of the many molecules contained in each sampling region. While the spectra therefore contain information about the compositions of the cell wall and the cytoplasm, respectively, in this context they function primarily as spectral fingerprints.

In order to investigate the ability of CARS spectroscopy to characterize spore heterogeneity, PCA was used to quantify the variation in the corrected CARS spectra of a

subset (n = 48) of the above *A. nidulans* intact spores. Spores included in the subset had minimum diameters that were able to be measured using image analysis software (see **Materials and Methods**). The first PC score of the spectrum of the edge of each spore is graphed against its minimum diameter in Figure 5.5. There is a weak but measurable CARS spectral variation with spore diameter, corresponding to a Pearson correlation coefficient of $\rho = -0.302$ with $R2 = 0.091$. In contrast, the calculated spectral variation of the center of each spore versus its diameter, which is not graphed, has a Pearson correlation coefficient of $\rho = 0.044$ with $R2 = 0.002$, which is about an order of magnitude less. From these calculations it is evident that there is a correlation between the spectrum of the cell wall and spore diameter, but not between the spectrum of the cytoplasm and the spore diameter. It can be concluded, then, that CARS spectroscopy can indeed provide a measure of spore heterogeneity, even when the spores under analysis are genetic clones of each other and are grown under the exact same conditions, as is the case here. It is to be expected then, that CARS may quantify even greater degrees of heterogeneity, such as those arising from disparate growth media and environments (see [22], for example).

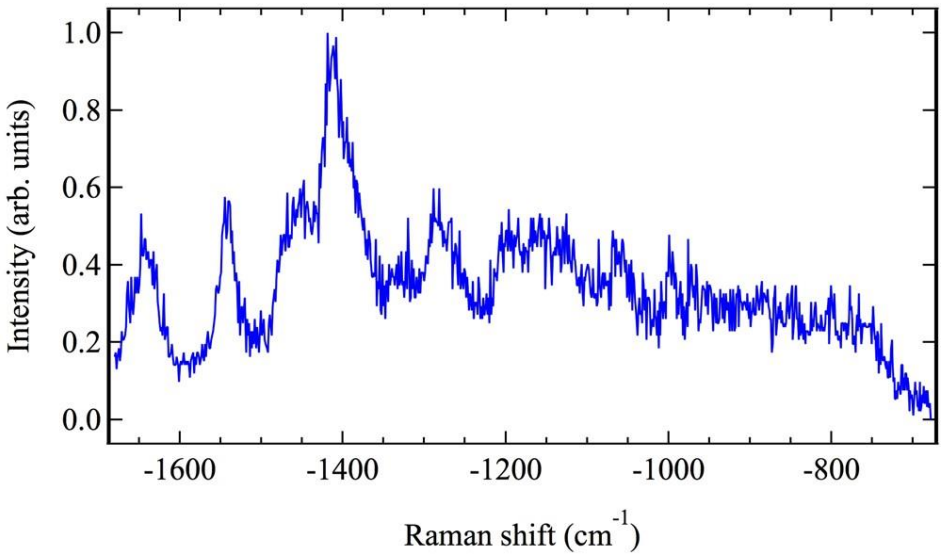

Figure 5.6. CARS spectrum of the cell wall of a single *Aspergillus nidulans* spore, taken on a sapphire substrate with an integration time of 0.1 s.

We have demonstrated that a transmissive CARS setup can rapidly measure and map fungal spores. While each measured CARS spectrum used in the above study was integrated for 1 s, we found that an integration time of 0.1 s was sufficient to obtain a recognizable *A. nidulans* CARS spectrum, as shown in Figure 5.6. Here, the measured raw spectrum was not processed in any way, so that the background non-resonant signal remains. Nevertheless, the characteristic peaks that identify the spectrum as belonging to the cell wall are clearly evident. In comparison, additional attempts to measure the spontaneous Raman spectrum using a continuous wave laser with 1064 nm wavelength necessitated an integration time of at least 100 s or more to obtain a recognizable spectral shape. The advantage of CARS over spontaneous Raman for the development of a rapid spore identification technique is therefore obvious. Moreover, we have conclusively shown that the transmissive CARS scheme detailed here differentiates even between the

cytoplasm and the cell wall of the spore itself. Not only does a CARS system have dramatic potential as a valuable tool for real-time identification of mold species, but it may also prove to be a powerful tool for mycologists to investigate biological processes which manifest differently within the cytoplasm and the cell wall of a fungal spore. We therefore predict that coherent Raman processes will find increased usage in the identification and study of fungi.

5.4. References

[1] Petrov, G. I. et al. Comparison of coherent and spontaneous Raman microspectroscopies for noninvasive detection of single bacterial endospores. PNAS. 2007; 104(19), 7776–7779.

[2] Scully, M. O. et al. FAST CARS: Engineering a laser spectroscopy technique for rapid identification of bacterial spores. PNAS. 2002; 99(17), 10994–11001.

[3] Beadie, G. et al. Towards a FAST CARS anthrax detector: coherence preparation using simultaneous femtosecond laser pulses. Opt. Commun. 2005; 244, 423–430.

[4] Pestov, D. et al. Single-shot detection of bacterial endospores via coherent Raman spectroscopy. PNAS. 2008; 105(2), 422–427.

[5] Pontecorvo, G., Roper, J. A., Hemmons, L. M., Macdonald, K. D. & Bufton, A. W. The genetics of Aspergillus nidulans. Adv. Genet. 1953; 5, 141–238.

[6] Hill, T. W. & Kafer, E. Improved protocols for Aspergillus minimal medium: trace element and minimal medium salt stock solutions. Fungal Genetics Reports 48, Article 8, https://doi.org/10.4148/1941-4765.1173 (2001).

[7] Shen, Y. et al. Picosecond supercontinuum generation in large mode area photonic crystal fibers for coherent anti-Stokes Raman scattering microspectroscopy. Scientific Reports. 2018; 8(1), 9526.

[8] Ghosal, S., Macher, J. M. & Ahmed, K. Raman microspectroscopy-based identification of individual fungal spores as potential indicators of indoor contamination and moisture-related building damage. Environ. Sci. Technol. 2012; 46(11), 6088–6095.

[9] Farazkhorasani, F. Raman and SERS studies of filamentous fungi. Masters Thesis, University of Manitoba, Winnipeg, Canada, (2014).

[10] Lieber, C. A. & Mahadevan-Jansen, A. Automated method for subtraction of fluorescence from biological Raman spectra. Appl. Spectrosc. 2003; 57(11), 1363–1367.

[11] De Gussem, K., De Gelder, J., Vandenabeele, P. & Moens, L. The Biodata toolbox for MATLAB. Chemometr. Intell. Lab. 2009; 95(1), 49–52.

[12] Vartiainen, E. M. Phase retrieval approach for coherent anti-Stokes Raman scattering spectrum analysis. JOSA B. 1992; 9(8), 1209–1214.

[13] Vartiainen, E. M., Rinia, H. A., Muller, M. & Bonn, M. Direct extraction of Raman line-shapes from congested CARS spectra. Optics Express. 2006; 14(8), 3622–3630.

[14] Kan, Y., Lensu, L., Hehl, G., Volkmer, A. & Vartiainen, E. M. Wavelet prism decomposition analysis applied to CARS spectroscopy: a tool for accurate and quantitative extraction of resonant vibrational responses. Optics Express. 2016; 24(11), 11905–11916.

[15] Yu, J. H. Regulation of development in Aspergillus nidulans and Aspergillus fumigatus. Mycobiology. 2010; 38(4), 229–237.

[16] Florance, E. R., Denison, W. C. & Allen, T. C. Jr. Ultrastructure of dormant and germinating conidia of Aspergillus nidulans. Mycologia. 1972; 64(1), 115–123.

[17] Winandy, L., Hilpert, F., Schlebusch, O. & Fischer, R. Comparative analysis of surface coating properties of five hydrophobins from Aspergillus nidulans and Trichoderma reseei. Scientific Reports. 2018; 8, 12033.

[18] Bull, A. T. Chemical composition of wild-type and mutant Aspergillus nidulans cell walls. The Nature of Polysaccharide and Melanin Constituents. J. Gen. Microbiol. 1970; 63, 75–94.

[19] Yoshimi, A., Miyazawa, K. & Abe, K. Cell wall structure and biogenesis in Aspergillus species. Biosci. Biotech. Bioch. 2016; 80(9), 1700–1711.

[20] Kuhn, P. J. & Trinci, A. P. J. Cell walls and membranes in fungi – an introduction in Biochemistry of cells and membranes in fungi (ed. Kuhn, P. J.) 1–4 (Springer, 1990).

[21] Cole, G. T. Models of cell differentiation in conidial fungi. Microbiol. Rev. 1986; 50(2), 95–132.

[22] Teertstra, W. R. et al. Maturation of conidia on conidiophores of Aspergillus niger. Fungal Genet. Biol. 2017; 98, 61–70.

6. CONCLUSIONS

In this dissertation, we apply Raman spectroscopy in identification and characterization of mold spores. The work in the chapter 2, 3, and 4, illustrate Shifted Excitation Raman Difference Spectroscopy (SERDS) has a distinct advantage over conventional background subtraction methods and that thus it is much more reliable and accurate.

In Chapter 2, we have used the SERDS technique to successfully retrieve the Raman spectra of conidia of three possible color phenotypes in *Aspergillus nidulans* (*A. nidulans*) and demonstrate the Raman spectra of *A. nidulans* conidia originate in the pigment molecules within the cell wall. In addition, vibrational fine-structure in the fluorescence at room temperature is observed. This unusual result may be due to the formation of flexible, long-lived molecular cages within the bio-polymer of the cell wall. And this effect may possibly play an important role in biological processes for which long-lived quantum coherence is required.

In Chapter 3, we have used SERDS technique to measure the Raman spectra of single conidial spores of 10 mold species. Consistent with the work in Chapter 2, the Raman signal originates from the melanin pigments bound within the highly cross-linked cell wall of the conidium. Moreover, the main features of the Raman spectrum correlate with the melanin bio-synthesis pathway.

In Chapter 4, we characterize the Raman spectra of melanin biosynthetic mutant strains of *A. fumigatus*, *C. neoformans*, and *A. nidulans* and used these spectra to elucidate the nature of the biosynthetic pathway of conidial melanin in *A. nidulans*. I find that the

dissimilarity between the *C. neoformans* and conidial *A. nidulans* Raman spectra excludes the possibility that the *A. nidulans* conidial pigment may be associated with the DOPA biosynthesis pathway. we also find that the *A. nidulans* conidial melanin cannot straightforwardly be classified as belonging to the DHN pathway.

Finally, we adopt coherent anti-Stokes Raman spectroscopy (CARS) to achieve rapid detection and chemical imaging of mold conidia and demonstrate that CARS could be a powerful tool and find increased usage in the identification and study of fungi.

APPENDIX A

RODA HYDROPHOBIN

The gene *rodA* of *A. nidulans* encodes a small, moderately hydrophobic polypeptide [1]. Classified as a hydrophobin protein, the polypeptide is involved in the formation of filamentous rodlets on the surface of the *A. nidulans* conidia [1-4]. The rodlet nanostructure is significantly hydrophobic and allows for more efficient dispersal of the conidium throughout the local environment [1, 2]. The deletion of the *rodA* gene abolishes the production of the corresponding polypeptide, which in turn inhibits the formation of the hydrophobic protein nanostructure on the surface of each conidium, and results in a comparatively smooth surface that is much less hydrophobic [1-4]. *A. nidulans* strains containing this deletion are termed Δ*rodA*, while their unmodified counterparts (which are otherwise considered isogenic with the mutants) are termed *rodA*$^{+}$.

REFERENCES

[1] Stringer, M.A., Dean, R.A., Sewall, T.C. & Timberlake, W.E. Rodletless, a new Aspergillus developmental mutant induced by directed gene inactivation. Genes and Development. 1991; 5, 1161-1171.

[2] Grunbacher, A., Throm, T., Seidel, C., Gutt, B., Rohrig, J., Strunk, T., Vincze, P., Walheim, S., Schimmel, T., Wenzel, W. & Fischer, R. Six hydrophobins are involved in hydrophobin rodlet formation in Aspergillus nidulans and contribute to hydrophobicity of the spore surface. PLOS ONE. 2014; 9(4), e94546.

[3] Claverie-Martin, F., Diaz-Torres, M.R. & Geoghegan, M.J. Chemical composition and electron microscopy of the rodlet layer of Aspergillus nidulans conidia. Curr. Microbiol. 1986; 14, 221-225.

[4] Zhao, L., Schaefer, D. & Marten, M.R.. Assessment of elasticity and topography of Aspergillus nidulans spores via atomic force microscopy. Applied and Environmental Microbiology. 2005; 70(2), 955-960.

APPENDIX B

CARS SIGNAL STRENGTH AS A FUNCTION OF TIME

In order to find a suitable beam power at which to take CARS measurements of *A. nidulans* spores, the integrated CARS spectrum (as calculated using the scheme in Materials and Methods above) was measured over a period of approximately 300 seconds for three different beam powers. The results are shown in Figure S2. The top, middle, and bottom curves correspond to beam powers of: 2.25 mW for the pump/probe and 1.2 mW for the Stokes; 1.65 mW for the pump/probe and 0.95 mW for the Stokes; and 1.07 mW for the pump/probe and 0.70 mW for the Stokes, respectively. Each curve is the averaged response of five individual spores. For each beam power level, the signal power remains relatively constant for about 10 s, after which the sample begins to experience thermal degradation, and the signal decreases. All of the CARS measurements used in this study were integrated for 1 s using a beam power of 1.65 mW for the pump/probe and 0.95 mW for the Stokes beam (corresponding to the middle curve). Consequently, our measurements do not suffer from thermal degradation of the sample. We note that the CARS signal strengths at t = 0 for each beam power level are consistent with a saturation model in the presence of strong absorption in the sample [1].

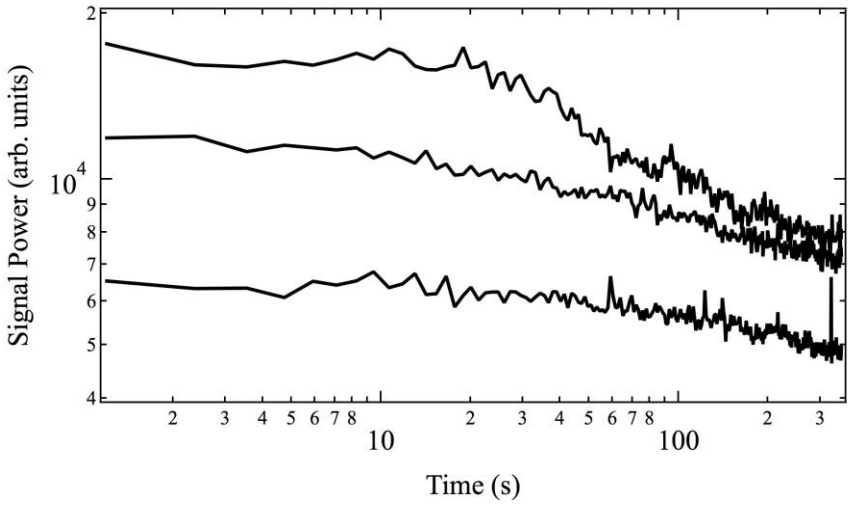

Figure A-1. Integrated CARS signal power as a function of time. The top, middle, and bottom curves correspond to beam powers of: 2.25 mW for the pump/probe and 1.2 mW for the Stokes; 1.65 mW for the pump/probe and 0.95 mW for the Stokes; and 1.07 mW for the pump/probe and 0.70 mW for the Stokes, respectively.

REFERENCES

[1] Zhi, M., *et al.* Concentration dependence of femtosecond coherent anti-Stokes Raman scattering in the presence of strong absorption. J. Opt. Am. B. 2007; 24(5), 1181-1186.